

AFIT/GAE/ENY/98J-02

WIND TUNNEL TESTING FOR DRAG REDUCTION OF AN AIRCRAFT LASER TURRET

THESIS

Presented to the Faculty of the Graduate School of Engineering
of the Air Force Institute of Technology
Air University
Air Education and Training Command
in Partial Fulfillment of the Requirements for the
Degree of Master of Science in Aeronautical Engineering

Christopher H. Snyder
Second Lieutenant, USAF

June 1998

Approved for public release; distribution unlimited

DTIC QUALITY INSPECTED 4

19980609 043

Disclaimer

The views expressed in this thesis are those of the author and do not reflect the official policy or position of the United States Air Force, the Department of Defense, or the United States Government.

Acknowledgements

This study would have been impossible to complete without the assistance of numerous individuals. I am very thankful for the guidance of Marc Masquelier, whose knowledge of aerodynamics and testing techniques proved invaluable. Similarly, Charlie McNeely's countless hours of help with the setup and operation in the AFIT 5-ft wind tunnel are sincerely appreciated. Dr. Milt Franke provided a great deal of advice throughout the entire process, and the additional assistance from Major Jeff Little and Captain Jeff Bons helped bring this document to its final form. I am also grateful for the excellent advice on data interpretation from Howard Emsley and Chris Murosky. The flow visualization skills of Gary Dale produced the oil traces that explained many phenomena in this study. Finally, none of this work would have taken place without funding from the Air Force Research Laboratory Sensors Directorate at Wright-Patterson AFB. I only hope that I can someday be as helpful to someone in my situation as the above individuals have been to me.

Table of Contents

	Page
Disclaimer	ii
Acknowledgements	iii
Table of Contents	iv
List of Figures	vii
List of Tables.....	x
List of Symbols	xi
Conventions.....	xiii
Abstract	xiv
<u>Chapter 1</u> <u>Introduction</u>	1
1.1 Background	1
1.2 Previous Research	3
1.3 Research Objective and Scope	5
<u>Chapter 2</u> <u>Theory</u>	7
<u>Chapter 3</u> <u>Experimental Hardware</u>	9
3.1 AFIT 1.5-m (5-ft) Wind Tunnel.....	9
3.2 Ground Plane.....	10
3.3 Instrumentation Cavity.....	12
3.4 Turret Model	13
3.5 Fairings and Splitter Plates.....	16

3.6	Load Cell Unit (LCU)	19
3.7	LCU Calibration Apparatus	20
3.8	Data Acquisition System.....	22
<u>Chapter 4</u>	<u>Experimental Procedures</u>	24
4.1	Calibration	24
4.1.1	Load Cell Unit (LCU)	24
4.1.2	Pressure Systems Inc. (PSI) System.....	26
4.2	Testing	26
4.3	Flow Visualization	27
4.3.1	Tufts	27
4.3.2	Oil Flow.....	28
<u>Chapter 5</u>	<u>Data Reduction</u>	30
5.1	Drag Coefficient.....	30
5.1.1	Drag Force, D	31
5.1.2	Air Density, ρ	31
5.1.3	Tunnel Velocity, V	32
5.1.4	Turret Frontal Area, S	33
5.2	Pressure Coefficient	34
<u>Chapter 6</u>	<u>Results and Discussion</u>	35
6.1	Flow Field Description.....	35
6.1.1	Clean Turret.....	35
6.1.2	Splitter Plates	41
6.1.3	Fairings.....	43

6.2	Pressure Distribution	46
6.2.1	Clean Turret.....	46
6.2.2	Splitter Plates	47
6.2.3	Fairings.....	49
6.3	Drag	51
6.3.1	Clean Turret.....	51
6.3.2	Splitter Plates	53
6.3.3	Fairings.....	55
6.4	Stability Properties	57
6.5	Effects of Testing Methods	61
6.5.1	Trip Strips.....	61
6.5.2	Cavity Opening	63
6.6	Results from Dynamic Response Pressure Transducers	66
6.7	Error Analysis	67
<u>Chapter 7</u>	<u>Conclusions and Recommendations</u>	70
References	74
Appendix A	Data Acquisition Apparatus	76
Appendix B	Load Cell Unit.....	78
Appendix C	Error Analysis	93
Vita	97

List of Figures

		Page
Figure 1.	Axis convention	xiii
Figure 2.	R/ILCT turret placement	2
Figure 3.	AFIT 1.5-m (5-ft) wind tunnel	9
Figure 4.	Ground plane and mounting system.....	11
Figure 5.	Instrumentation cavity, turret, and cover ring	12
Figure 6.	Static pressure tap and transducer locations.....	14
Figure 7.	Interior of turret and instrumentation cavity	15
Figure 8.	Small and large splitter plates	17
Figure 9.	Splitter plate attachment points	18
Figure 10.	Small and large fairings.....	19
Figure 11.	Load Cell Unit (LCU)	20
Figure 12.	Calibration stand and cable	21
Figure 13.	Oil applied to turret, wind off.....	29
Figure 14.	Oil flow, 55 m/s (180 ft/s), front view of turret	36
Figure 15.	Horseshoe vortex representation, front view of turret.....	37
Figure 16.	Horseshoe vortex model.....	37
Figure 17.	Oil flow, 55 m/s (180 ft/s), side view of turret.....	39
Figure 18.	Oil flow, 55 m/s (180 ft/s), rear view of turret.....	40
Figure 19.	Tuft run, 55 m/s (180 ft/s), side view of turret.....	40
Figure 20.	Tuft run, 55 m/s (180 ft/s), small splitter plate installed	42

Figure 21.	Tuft run, 55 m/s (180 ft/s), small fairing installed	44
Figure 22.	Tuft run, 55 m/s (180 ft/s), large fairing installed.....	45
Figure 23.	Pressure distribution, similar shapes	46
Figure 24.	Pressure distribution, small splitter plate installed.....	48
Figure 25.	Pressure distribution, large splitter plate installed	49
Figure 26.	Pressure distribution, small fairing installed.....	50
Figure 27.	Pressure distribution, large fairing installed.....	51
Figure 28.	Drag coefficient comparison, similar shapes	52
Figure 29.	Drag coefficient comparison, splitter plates installed	54
Figure 30.	Drag coefficient comparison, fairings and splitter plates.....	55
Figure 31.	Side force coefficient comparison, fairings and splitter plates	57
Figure 32.	Yaw moment coefficient comparison, fairings and splitter plates	59
Figure 33.	Drag comparison, turret with trip strips installed and removed.....	62
Figure 34.	Drag comparison, instrumentation cavity open and closed.....	64
Figure 35.	Oil flow, 55 m/s (180 ft/s), cavity open	65
Figure 36.	Oil flow, 55 m/s (180 ft/s), cavity closed.....	66
Figure 37.	Uncertainty in drag coefficient measurements.....	68
Figure 38.	Uncertainty in pressure coefficient measurements.....	69
Figure 39.	Individual load cell placement within the LCU	78
Figure 40.	Drag check-load prior to testing	82
Figure 41.	Drag check-load following test completion	82
Figure 42.	Negative F_x calibration	83
Figure 43.	Negative F_x (high) calibration	83

Figure 44.	Positive M_y calibration (negative F_x applied)	84
Figure 45.	Positive M_y calibration (negative F_x {high} applied)	84
Figure 46.	Positive F_x calibration	85
Figure 47.	Positive F_x (high) calibration.....	85
Figure 48.	Negative M_y calibration (positive F_x applied).....	86
Figure 49.	Negative M_y calibration (positive F_x {high} applied).....	86
Figure 50.	Negative F_y calibration.....	87
Figure 51.	Negative F_y (high) calibration	87
Figure 52.	Negative M_x calibration (negative F_y applied).....	88
Figure 53.	Negative M_x calibration (negative F_y {high} applied).....	88
Figure 54.	Positive F_y calibration	89
Figure 55.	Positive F_y (high) calibration.....	89
Figure 56.	Positive M_x calibration (positive F_y applied)	90
Figure 57.	Positive M_x calibration (positive F_y {high} applied)	90
Figure 58.	Negative M_z calibration.....	91
Figure 59.	Positive M_z calibration	91
Figure 60.	Positive F_z calibration	92

List of Tables

	Page
Table 1. Side force and yaw moment coefficient slopes (vs. β)	58
Table 2. Load cell output voltage definitions.....	79
Table 3. Drag coefficient error	94
Table 4. Pressure coefficient error	96

List of Symbols

<u>Symbol</u>	<u>Definition</u>
[A]	calibration coefficient matrix
ABL	Airborne Laser
A/D	analog to digital
AFIT	Air Force Institute of Technology
AFRL/SN	Air Force Research Laboratory, Sensors Directorate
C_D	drag coefficient
C_n	yaw moment coefficient
$C_{n\beta}$	slope of yaw moment coefficient vs. sideslip angle
C_p	pressure coefficient
C_y	side force coefficient
$C_{y\beta}$	slope of side force coefficient vs. sideslip angle
D	drag force
dia	diameter
E_0 through E_7	individual load cell voltages
EC_1 through EC_6	load cell unit combined voltages
{EC}	vector of load cell unit combined voltages
F_x, F_y, F_z	forces in the x-, y-, and z-directions, respectively
{F}	vector of six loading components
FFT	Fast Fourier Transform
KTAS	Knots True Airspeed

LCU	load cell unit
M	Mach number
M_x, M_y, M_z	moments about the x-, y-, and z-axes, respectively
P_{atm}	atmospheric pressure
P_{local}	static pressure at location on turret surface
P_{total}	total (stagnation) pressure
P_{tun}	static pressure measured in tunnel test section
PSI	Pressure Systems, Inc.
q	dynamic pressure
R	specific gas constant
Re_D	Reynolds number (based on diameter)
R/ILCT	Reconnaissance/Intelligence Laser Communication Terminal
S	frontal area of turret
T	temperature
V	wind tunnel velocity
V_{corr}	wind tunnel velocity, corrected for blockage
β	sideslip angle
ϵ_t	test section blockage correction
ρ	density

Conventions

Axes

x	Positive out the nose of the aircraft/device
y	Positive out the right wing
z	Positive down

Force Coefficients

C_D	Drag coefficient
C_y	Side force coefficient

Moment Coefficient

C_n	Yaw moment coefficient, positive for nose right
-------	---

Angles

β	Angle of sideslip, positive for cw rotation of relative wind
---------	--

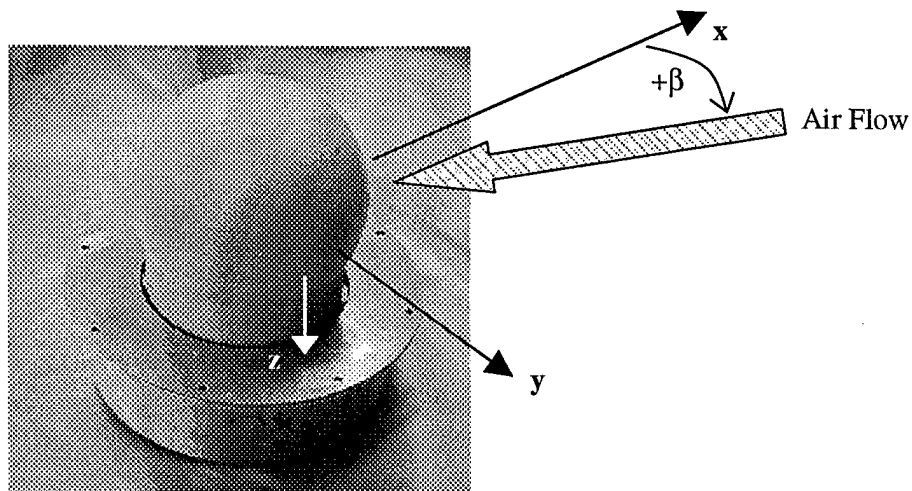


Figure 1. Axis convention (Alexander, 1991: IV-5)

Abstract

This study investigated the use of aft-mounted fairings and splitter plates to reduce the drag of a half-scale aircraft laser turret. Forces, moments, and pressure distributions were measured in the AFIT 1.5-m (5-ft) wind tunnel at Reynolds numbers between 3×10^5 and 9×10^5 based on the turret diameter. Oil traces indicated the nature of the flow near the surface of the unmodified turret and the surrounding area. Tufts placed on the turret, fairings, and splitter plates showed changes in separation regions when configurations were changed. The flow around the turret was characterized by dominant vortices shedding from the top of the turret and a large trailing wake of vorticity. Splitter plates were ineffective in reducing drag as a result of the strong flow over the top of the turret. A small fairing reduced baseline drag by 49% but was unable to produce attached flow near the turret. A large fairing eliminated nearly all separation regions and reduced baseline drag by 55%.

WIND TUNNEL TESTING FOR DRAG REDUCTION OF AN AIRCRAFT LASER TURRET

Chapter 1 - Introduction

1.1 Background

Airborne lasers were originally created to be high-energy weapon systems capable of rapid deployment and deadly accuracy. Recently, interest has expanded to using airborne lasers in a communications role, and the Air Force Research Laboratory Sensors Directorate (AFRL/SN) of Wright-Patterson Air Force Base, Ohio, is managing a program to design and test this capability. The objective of the Reconnaissance/Intelligence Laser Communication Terminal (R/ILCT) program is to develop and demonstrate long-range, high bandwidth laser communications between two high altitude aircraft. This technology would provide the capability to relay reconnaissance or intelligence information from a forward location via a secure data link. In addition to communications between two aircraft, the R/ILCT would also be capable of communications with ground stations and, with future advances, space-based platforms.

Two testbed aircraft will be modified and flown in various mission simulations during the R/ILCT flight test phase. The required flight test conditions include a 1.5-hour

period of sustained flight operations at 12,000 m (40,000 ft) at approximately 400 knots true airspeed (KTAS). To meet these requirements, two decommissioned Air Force business-class-size jet aircraft, T-39 Sabreliners, have been designated for testing the R/ILCT. The major modification to the aircraft exterior is the installation of a 0.46 m (1.5 ft) diameter turret to house the laser system. The turret is to be placed underneath the aircraft along its centerline and even with the wing root leading edge in the existing crew escape hatch. Figure 2 shows the placement of the turret as well as a general schematic of the R/ILCT system.

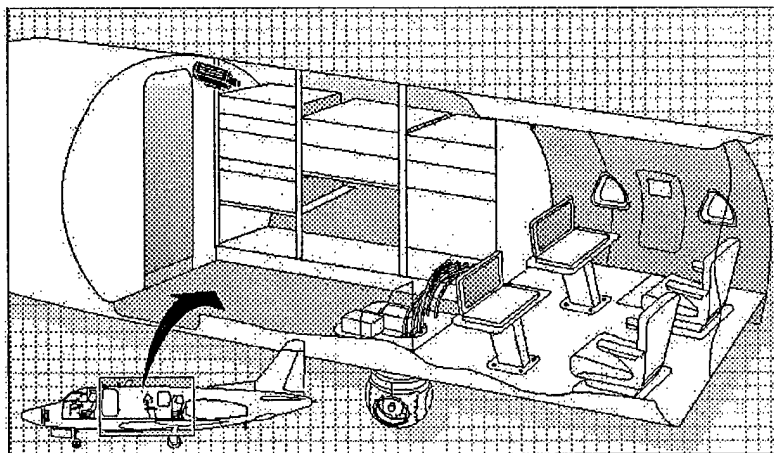


Figure 2. R/ILCT turret placement

During a typical high-altitude T-39 mission, a large portion of the mission time is consumed in the climb and descent phases. When placing the R/ILCT turret on the fuselage exterior, an important factor becomes the amount of drag created by the modification. Without some method of streamlining, the turret's spherical shape will

induce a large drag penalty, extend the time spent in the climb and descent phases, and increase the fuel flow once at altitude. This drag penalty significantly decreases the effective mission time at the desired cruise altitude, and drag reduction becomes a key concern for the R/ILCT program.

Drag reduction is not the only important factor in such a fuselage modification, however. In this application, the turret is placed forward of the aircraft's center of gravity, and its aerodynamics can significantly affect the stability and control of the aircraft. Consequently, predicting the impact of the R/ILCT turret and any associated drag reduction devices on the aircraft handling qualities becomes an important requirement as well.

1.2 Previous Research

A significant amount of research has been dedicated to testing aerodynamic shapes (cylinders, spheres, airfoils, etc.) and attempting to produce efficient means of reducing the drag produced by each. Most of these tests are carried out on high aspect ratio (length to width) shapes placed between widely spaced endplates or wind tunnel walls. These configurations approximate infinite length shapes and the resulting flows are two-dimensional in nature. Wall effects, normally encountered near an object's attachment to a plate or wind tunnel wall, often become negligible as a result of these infinite lengths.

When one of the shapes mentioned previously is modified to a low aspect ratio and tested in a finite configuration, the flow is transformed into a complex three-dimensional velocity field and is usually impossible to predict at turbulent Reynolds numbers with closed-form solutions from fluid dynamics theory. Wall effects, boundary layers, and vorticity about multiple axes contribute to the complexity of the flow, just to name a few. Aircraft turrets such as the one considered in this study are typically spherical in shape and blended to a cylindrical base near the point of attachment to the aircraft. In a configuration such as this, two-dimensional drag results offer little in the form of true comparisons and must be examined carefully before making any correlations with certainty. In contrast, three-dimensional tests of similar shapes or configurations prove extremely valuable in determining differences in the flow field and drag characteristics for a turret shape. These results are correspondingly difficult to locate, since testing on turret shapes has been limited and the results from many such tests done over two decades ago are simply unavailable.

Several tests of similar turret shapes were carried out in the mid-1970s at Wright-Patterson AFB in support of the Airborne Laser (ABL) program. In these tests, emphasis was placed on reducing the drag of the turret and minimizing the aerodynamic forces, torques, and vibrations placed on a turret with an open viewing port (Mullane, 1975: 2). Many methods of drag reduction were tested, including fore and aft fairings, side fairings, boundary layer suction, mass flow injection, and scoops and channels placed near the top of the turret. One test determined the lowest drag configuration to consist of the turret, forward ramped shell, and aft fairing, which decreased the drag by 30% compared to the

lone turret configuration (Walterick and Van Kuren, 1975: 39). Another test realized a 50% reduction in torque on the turret by utilizing flow injection at the base of the viewing port (Mullane, 1975: 24).

Key differences between earlier configurations and the turret tested in this study made comparisons with previous results difficult. Laser technology has advanced to the level of using a window over the viewing area that matches the curvature of the turret itself. Also, previous turrets were tested on a cylindrical surface approximating the fuselage of a large transport aircraft; this study examined a turret to be mounted on the flat underside of the T-39 Sabreliner. Differences in flat and curved wall interactions most likely affected the aerodynamic characteristics of the turret and any associated drag reduction devices. Finally, more stringent operational limits have been placed on the size of any modifications added to the testbed aircraft. The laser is required to have an unobstructed view of all areas forward of the turret centerline. With a viewing window several inches wide, the cross-sectional area available to any drag reduction device has been reduced below the frontal area of the turret. Thus, any modification placed behind the turret will be non-ideal from an aerodynamic standpoint (compared to an object that extends to the sides of the turret, for example).

1.3 Research Objective and Scope

This study investigated the complex aerodynamics of a laser turret model by measuring forces, moments, and pressures acting on the turret. The objective was to

characterize the flow field around the turret, identify regions of separation, and determine a passive drag reduction technique that improved flow quality near the turret while meeting the viewing requirements of the laser. Stability properties of each configuration were tested as well to predict any potentially hazardous conditions that could occur while flight testing such fuselage modifications.

Since all testing was carried out in the low-speed AFIT 1.5-m (5-ft) wind tunnel, conditions matching those of the flight test ($Re_D=2.0 \times 10^6$ and $M=0.7$ at cruise) could not be attained. Wind tunnel tests were conducted at a 0° angle of attack, and Reynolds numbers in the range of 3×10^5 to 9×10^5 based on the turret diameter were recorded (corresponding to a maximum Mach number of 0.19). Although low-speed testing did not provide ideal comparisons with the flight conditions, the large size of the AFIT 1.5-m (5-ft) wind tunnel allowed for testing and flow visualization of relatively large (half-scale) models. The relative performances of drag reduction devices versus the baseline (clean) turret indicated the drag savings that could be expected on the testbed aircraft at subsonic speeds. A further discussion of the applicability of this study to flight test conditions can be found in Chapter 7. When examining stability properties, each configuration was only tested at sideslip angles of 5° and smaller. Results in this area did not represent the full range of sideslip angles encountered in flight, but structural and safety concerns limited this phase of the testing to small angles.

Chapter 2 - Theory

This study examined the three-dimensional flow over a spherical turret with a cylindrical base mounted on a flat plate. The “short and fat” shape of the turret made it a bluff body, and the drag on such objects is usually dominated by pressure drag (Hoerner, 1965: 3-5). Pressure drag results from forces acting normal to the surface of a body, in contrast to skin friction drag that results from tangential forces. The primary cause of pressure drag observed in this study was boundary layer separation, in which smooth flow attached to a body meets an adverse pressure gradient and eventually cannot overcome the increasing pressure. When this occurs, the formerly attached flow detaches from the body surface and forms a wake of swirling vortices behind the body. This wake is at a lower pressure than the flow near the front of the body and the pressure differential results in pressure drag.

In the case of a cylinder oriented between two flat plates, the vortices are shed from the sides in an alternating fashion and form a vortex system known as a vortex street. These vortices have axes parallel to the cylinder’s axis and rotate in opposite directions while moving downstream. In three-dimensional flows, vortex systems can form about multiple axes, interact with one another, and create extremely complex flow fields. For example, the flow around a sphere becomes unstable as the Reynolds number is increased. Eventually, vortices are carried away in irregular packages and the line of separation moves back and forth along the surface of the sphere in an irregular, unsteady fashion as well (Hoerner, 1965: 3-5).

The main strategy in reducing the drag on bluff bodies is to decrease the size or magnitude of the turbulent, low-pressure wake behind the body. Two such drag reduction methods were tested in this study: splitter plates and fairings. Splitter plates are essentially two-dimensional structures (thin walls) placed behind a bluff body along the centerline of the vortex street. Their purpose is to reduce the motion of the vortex street and prevent the two systems of vortices from mixing as much as possible. This breaks the large zone of vorticity into smaller zones and reduces the strength of the low-pressure wake behind the bluff body. Fairings take this approach a step further. In addition to breaking large areas of wake vorticity into smaller, less powerful vortices, fairings are designed to delay or even eliminate separation from the bluff body. If separation still occurs, though, fairings usually provide streamlined shapes for the flow to reattach to, and only a minimal turbulent wake forms behind the bluff body.

Chapter 3 - Experimental Hardware

3.1 AFIT 1.5-m (5-ft) Wind Tunnel

All testing was carried out in the AFIT 1.5-m (5-ft) wind tunnel, constructed in 1921 at McCook Field in Dayton, Ohio. In 1928, it was moved to its current location in Building 19, Wright-Patterson Air Force Base, Ohio, where it continues to be the oldest operating wind tunnel in the country (Wolf, 1995:3). Shown in Figure 3, this semi-open-circuit-type tunnel is primarily constructed of wood and has a 1.5-m (5-ft) diameter test section that is 5.5 m (18 ft) in length. Building 19 completely encloses the tunnel, and room air mixes with discharged air before being drawn into the air straightener and intake bell. Four 400-HP DC electric motors drive the two 3.6-m (12-ft) counter-rotating fans to produce a maximum velocity of 89 m/s (293 ft/s). This corresponds to a maximum unit Reynolds number of approximately $5.95 \times 10^6 / \text{m}$ ($1.82 \times 10^6 / \text{ft}$).

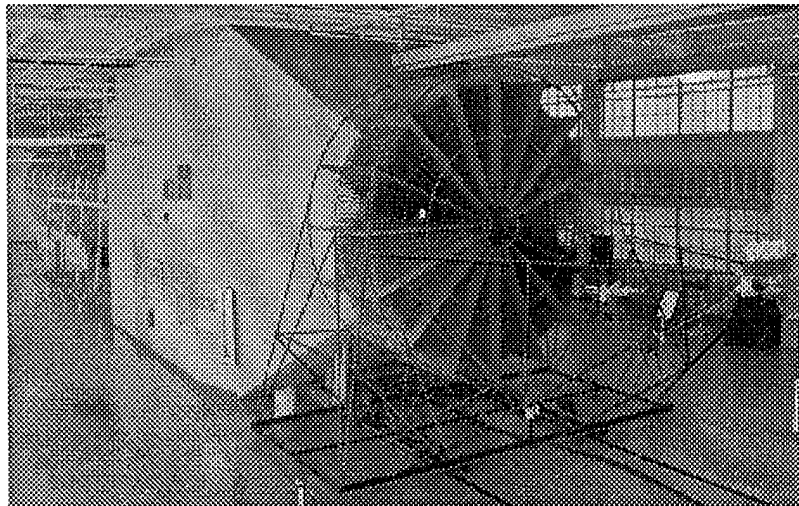


Figure 3. AFIT 1.5-m (5-ft) wind tunnel

A digital pressure transducer connected to eight static ports measures the static pressure in the test section. These ports are located at the inlet to the test section and are spaced evenly around its circumference. The dynamic pressure in the test section (tunnel q) is determined by calculating the difference between the total pressure of the flow (atmospheric) and the static pressure measured at the inlet to the test section. The desired flow velocity, calculated directly from the dynamic pressure, may be obtained by varying the coarse and fine speed controls of the DC motors.

3.2 Ground Plane

A rectangular wood platform (ground plane) was placed in the test section to simulate the predominantly flat underside of the T-39 and provide a mounting system for the model and its instrumentation. An elliptical leading edge reduced the turbulence created as the flow split above and below the ground plane, and the sides of the plane were tapered to match the curvature of the wind tunnel where it was attached. Four aluminum brackets secured the edges of the ground plane to the tunnel walls. As an extra precaution against the ground plane lifting and breaking free of its mounts, safety wire anchored the leading edge of the plane to the floor of the wind tunnel.

The ground plane was originally constructed for a previous research study. Modifications for this study consisted of a large hole to accommodate the instrumentation cavity and four sets of threaded holes to mount calibration stands to the ground plane. Shown in Figure 4, the 0.32-m (12.5-in) diameter cavity hole was located 1.17 m (46 in) aft of the leading edge and centered between the left and right sides of the ground plane.

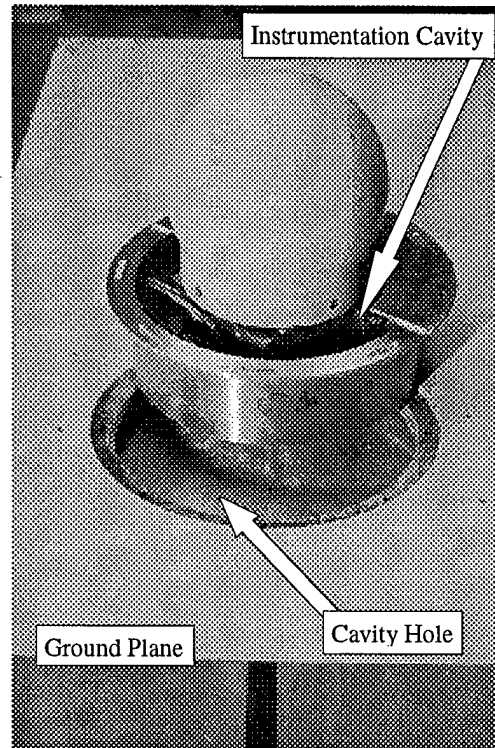


Figure 4. Ground plane and mounting system

A groove around the cavity hole held the top lip of the instrumentation cavity below the surface of the ground plane, and an aluminum ring with threaded holes was fastened directly beneath the groove. Since the thickness of the ground plane had been reduced in the vicinity of the cavity hole, the ring provided reinforcement in this area as well as strong threads with which to tighten the entire cavity/model assembly into place.

The remaining modification to the ground plane was the addition of four sets of mounting holes for the calibration stands. The sets of holes were located upstream,

downstream, and to each side of the model. This allowed for calibration in both x-directions (positive and negative drag) as well as both y-directions (positive and negative side forces). A threaded insert in each hole provided greater strength and stability when the calibration stands were bolted to the ground plane.

3.3 Instrumentation Cavity

The instrumentation cavity, essentially an aluminum inverted top hat, served as a mounting platform for the load cell unit (LCU), which, in turn, was mounted to the turret model (see Figure 5). The interior of the cavity provided a wind-free environment within the wind tunnel to make electrical and pneumatic connections to the pressure measurement system as well as electrical connections to the LCU. The LCU was centered

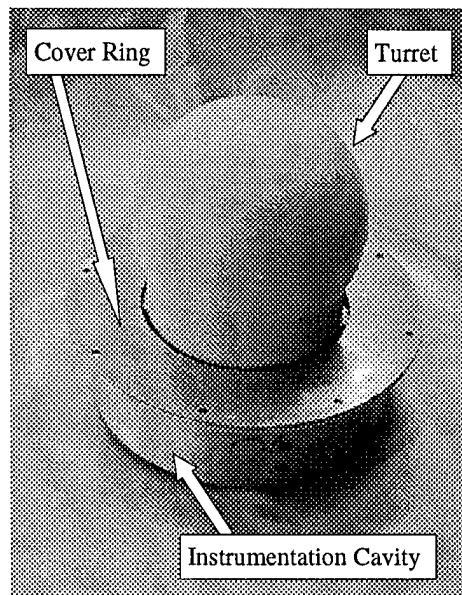


Figure 5. Instrumentation cavity, turret, and cover ring

within the instrumentation cavity and mounted to the cavity base. Instrumentation wires and tubes connected to the model ran through a hole in the cavity wall to the data acquisition systems in the wind tunnel control room. This hole was placed facing downstream and plugged with modeling clay to avoid airflow into the cavity. Around the top of the instrumentation cavity, a lip extended outward to mount the cavity onto the ground plane. Mounting bolts passed through arc-shaped slots in the lip that allowed for $\pm 5^\circ$ rotation of the cavity/model assembly.

An aluminum cover ring surrounded the base of the turret model and covered the exposed portions of the instrumentation cavity. When placed in the circular groove in the ground plane, the surface of the ring was flush with the surface of the ground plane. A 0.48-cm (3/16-in) gap between the ring and the turret allowed deflection of the turret during testing. This small gap made the ring's inner diameter too small to clear the spherical portion of the turret, however. To allow access to the instrumentation cavity without first removing the turret, the ring was separated into two semicircular pieces. Countersunk holes in the ring placed the flat-head mounting bolts flush with the surface of the ground plane when tightened.

3.4 Turret Model

The turret model was a half-scale model of the proposed turret housing the laser optics on the T-39 Sabreliner. Created from a large block of laminated mahogany, the turret was a 0.23-m (9.25-in) diameter sphere blended to a 0.2-m (8-in) diameter

cylindrical base. A large cylindrical cutout within the model provided for the routing of pressure tap tubing as well as the mounting of the turret to the LCU.

Eleven static pressure taps were installed in the spherical portion of the turret using 0.102-cm (0.040-in) outer diameter stainless steel tubing (see Figure 6). Six taps were aligned with the x-z (vertical) plane, beginning with the stagnation point in front and running over the top of the turret in 30° intervals. Five taps were placed in the x-y (horizontal) plane around the largest diameter of the sphere, beginning with 90° aft of the stagnation point and continuing rearward in 15° intervals. In addition, four Endevco piezoresistive pressure transducers were installed in the same horizontal plane as the five static taps. Three of the transducers were spaced evenly between the static taps at positions of 97.5°, 112.5°, and 127.5° aft of the stagnation point, respectively. The remaining transducer was positioned in the same plane at 127.5° aft of the stagnation point on the opposite side of the model.

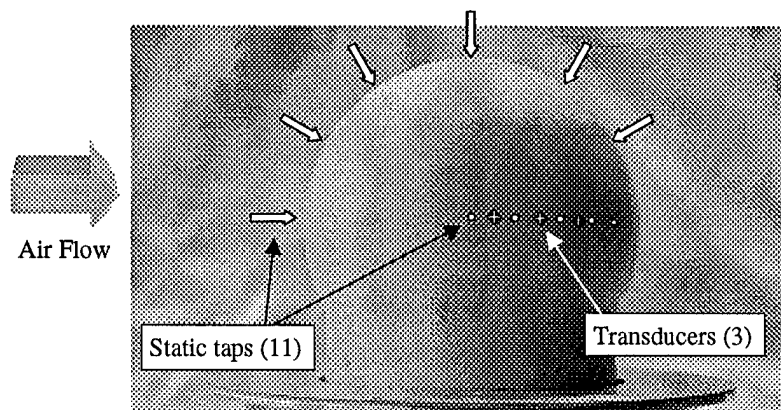


Figure 6. Static pressure tap and transducer locations

An aluminum mounting cylinder secured the turret model to the LCU. Bolts running vertically through the cylinder tightened the cylinder to the LCU. When the model was slid onto the cylinder, bolts running radially through countersunk holes in the model screwed into threaded holes in the cylinder. This mounting system, shown in Figure 7, connected the turret model to the LCU rigidly and exclusively. Pressure tap tubing and wires passed from the upper portion of the turret through a hole in the aluminum mounting cylinder and into the instrumentation cavity.

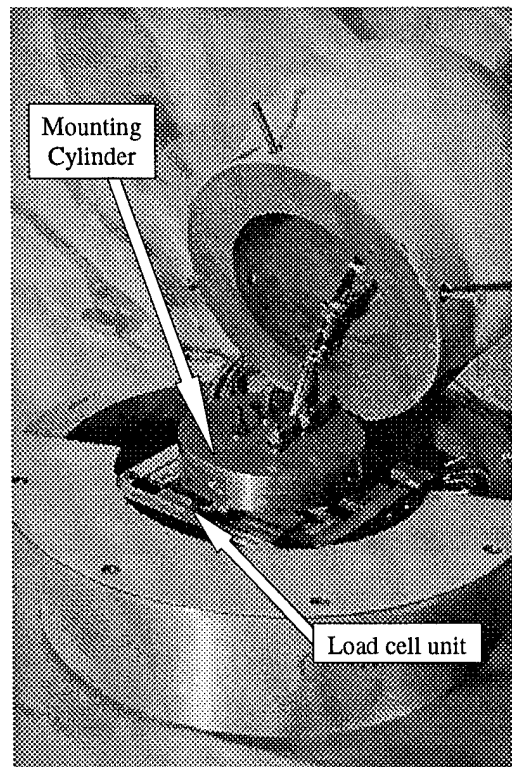


Figure 7. Interior of turret and instrumentation cavity

Three fairing/splitter plate mounting holes were located on the rear side of the model in the x-z plane. One hole served as a receptacle for a common pin placed at the same location on each fairing and splitter plate. The other two holes were fitted with brass threaded inserts. The lower threaded hole was a common mounting point for the small fairing and splitter plate. Similarly, the upper threaded hole was used to attach the large fairing and splitter plate. The remaining point of attachment for the fairings and splitter plates was a semicircular aluminum band recessed into the base of the turret model. Bolts secured the aluminum band to the base leading edge of a fairing or splitter plate. After placing the band in its matching recess in the turret, bolts mounted the band and attached fairing or splitter plate to the turret. Once tightened, the band gave lateral support to the fairing or splitter plate that the other three points of attachment could not provide.

3.5 Fairings and Splitter Plates

An important constraint placed on any modifications to the actual turret was the maximum look angle available to the laser system. This angle, measured from the front of the aircraft to the center of the laser optics window, was the largest angle the turret could rotate with an unobstructed view from the viewing window. Since the laser optics window had a 60° field of regard, an extra 30° of viewing area was required for a given look angle (which was referenced to the center of the window). Two sizes of fairing and splitter plate models simulated different look angles for the actual laser system. The small and large splitter plates shown in Figure 8 allowed look angles in the x-z plane (elevation) of 120° and 90°, respectively. Both splitter plates were 0.95-cm (3/8-in) thick

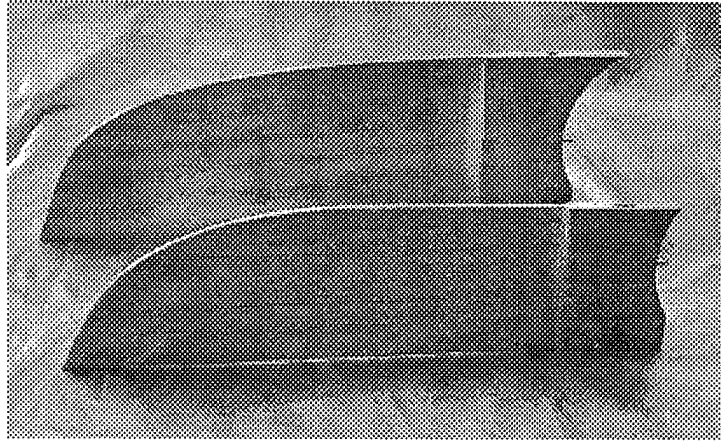


Figure 8. Small and large splitter plates

aluminum, 2.6 turret diameters in length, allowing a look angle in the x-y plane (azimuth) of nearly 150° . The plates were cantilevered from the turret model 0.95 cm (3/8 in) above the ground plane to ensure they would not contact the ground plane and invalidate the force data. Two triangular aluminum braces connected the bases of the splitter plates to the aluminum semicircular ring and provided increased lateral support (see Figure 9).

Since the splitter plates were cantilevered on the back of the turret, a primary concern was designing plates that would be heavy enough to withstand the aerodynamic loads but not too heavy for the LCU to support. The combination of the positive pitching moment on the turret from the weight of the splitter plate and the drag force at higher velocities would tend to place the trailing edge of the splitter plate against the ground plane. To avoid this problem, the thickness of both splitter plates was reduced to 0.48 cm (3/16 in) from the trailing edge to 0.65 diameters aft of the leading edge. The leading

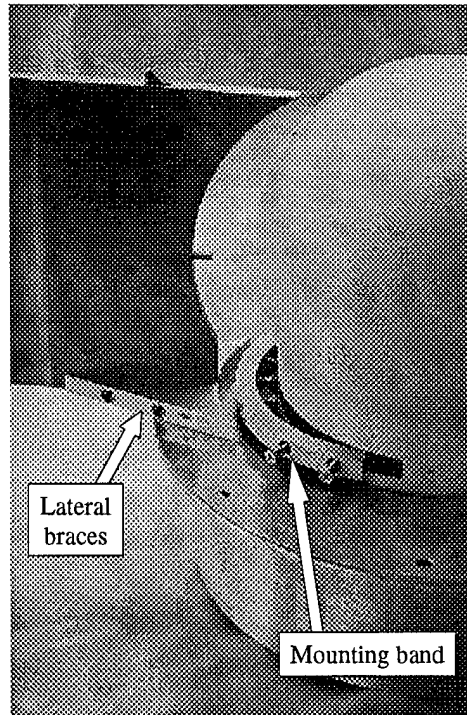


Figure 9. Splitter plate attachment points

edge thickness was preserved to avoid using thinner and weaker mounting bolts. With this modification, the weight of both splitter plates was reduced considerably and contact with the ground plane did not occur.

The small and large blended fairings were manufactured from Renboard, a synthetic mahogany material. Since the aerodynamic loads on the cantilevered fairings were unknown, Renboard was chosen for its higher strength than mahogany, yielding an added safety factor. Shown in Figure 10, the small and large fairings allowed 120° and 90° look

angles, respectively. Both fairings were the same length, cantilevered the same distance above the ground plane, and shared the same three attachment points to the turret as listed previously for the splitter plates. In the case of the fairings, however, each was wide enough to place threaded inserts in its base to attach to the semicircular aluminum band; no mounting modifications were necessary. This large width resulted in substantial weight, and the interiors of the fairings were manually milled out, leaving shells with an average 1.6-cm (5/8-in) wall thickness. As in the case of the splitter plates, this greatly decreased the weight and prevented contact with the ground plane.

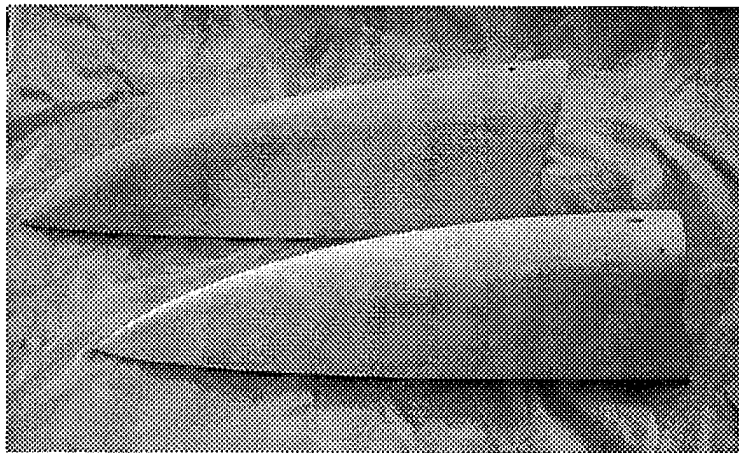


Figure 10. Small and large fairings

3.6 Load Cell Unit (LCU)

The load cell unit (LCU), originally constructed for a previous thesis study, was used to determine the three forces and three moments acting on the turret under each configuration (see Figure 11). Eight load cells were arranged to give symmetric loading

in each direction. Each load cell had a sensitivity of ± 0.08 mm (0.003 in) over the load cell range of 111 N (25 lb_f). The upper x-y plane of the LCU consisted of four load cells oriented to measure F_x and F_y (two load cells for each force) and M_z (all four load cells). The four lower load cells acted as legs to support the upper portion of the LCU, which was in turn connected to the turret model assembly. All four lower load cells measured M_x , M_y , and F_z . Four bolts mounted the LCU to a 0.95-cm (3/8-in) thick steel plate that was in turn mounted to the cavity base. The theory of the LCU and the details of its calibration and use are presented in Appendix B.

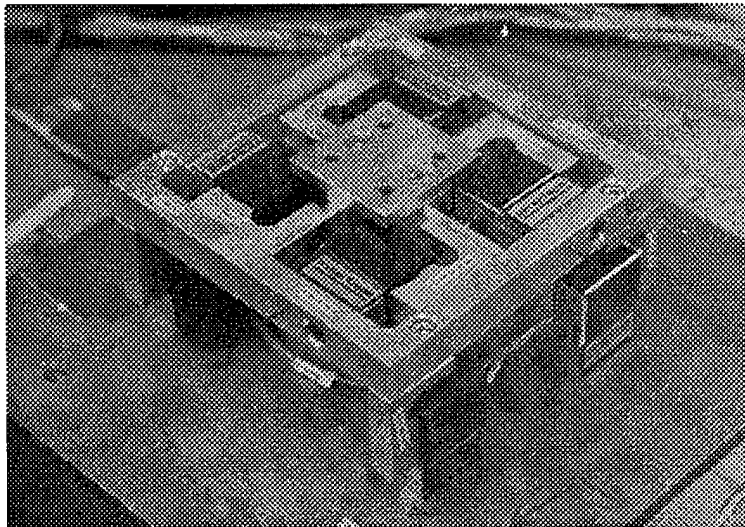


Figure 11. Load Cell Unit (LCU)

3.7 LCU Calibration Apparatus

Two calibration stands were constructed for this study to apply known forces and moments to the installed turret model. These stands used simple hanging weights to load

the model and determine the corresponding responses from the LCU. Each stand was essentially two steel beams mounted on a steel base plate (see Figure 12). The plate was secured to the ground plane in one of the four calibration locations discussed in Section 3.2. The steel beams had a square “U” cross section that allowed special slider mounts to be positioned and tightened at any point along their length. Two pulleys transferred the vertical force of the hanging weight stack to a horizontal force on the turret model.

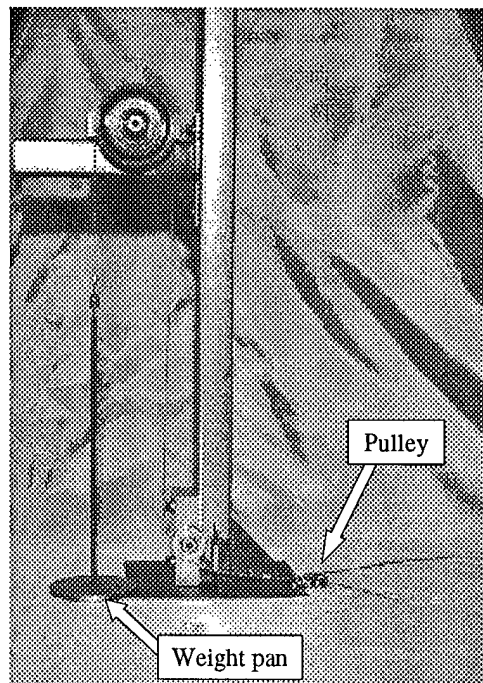


Figure 12. Calibration stand and cable

A 0.16-cm (1/16-in) diameter steel cable looped around the turret and a second length ran through the calibration setup to a light aluminum weight pan. A small pulley connected the two cables to give straight, consistent pulls and reduce side loads on the

turret when pulling axially. Tygon tubing enclosed the cable in contact with the model to protect against damage to the surface of the model. Moving the adjustable pulley on the vertical beam changed the height at which the cable pulled on the turret, and the other adjustments on the calibration stand were used to take up any slack in the cable.

3.8 Data Acquisition System

The data acquisition system measured and recorded the forces, moments, and pressures acting on the model as well as freestream flow parameters. All data was acquired in LABVIEW, a graphical programming package for data acquisition installed on a Zenith Pentium 133 MHz Z-station. The LCU signals were processed through Endevco signal conditioners, which provided a clean and steady excitation voltage to the LCU. Two Endevco power supplies powered the eight signal conditioners, and a gain of 50 was selected on the front of each signal conditioner. The signal conditioners were connected to a National Instruments data acquisition board, at which point the signal was converted from analog to digital. An AT-GPIB interface card was installed in the Zenith Z-station and connected to the data acquisition board to give LABVIEW access to the digital signals.

A Pressure Systems Incorporated (PSI) automated pressure measurement system determined the static pressure at various locations on the turret surface. The PSI system was a microcomputer-based, stand-alone system that LABVIEW accessed via the AT-GPIB interface card. The static taps were connected to an electronic pressure scanner placed in the cavity beneath the model. Signals from the pressure scanner passed to an

A/D converter and into the PSI system processor. A pressure calibration unit applied known pressures to the pressure scanner and automatically generated calibration curves for each tap.

A Hewlett-Packard signal analyzer measured the dynamic response from the four piezoresistive pressure transducers mounted in the model. This analyzer was placed in Fast Fourier Transform (FFT) mode to identify any dominant frequencies of the flow in the separated regions. The signal from each pressure transducer was passed through an Endevco signal conditioner, and an Endevco power supply powered all four signal conditioners. The signal conditioners were set to a gain of 50 and connected directly to the HP signal analyzer.

An MKS differential pressure transducer coupled with an MKS digital power supply readout determined the dynamic pressure of the flow within the test section. This information was converted in LABVIEW to give a real-time display of the test section flow velocity. Air temperature within the tunnel was measured with an Omega thermocouple and displayed in LABVIEW through an Omega thermocouple indicator. A digital mercury barometer located in the tunnel building measured barometric pressure, and this value was manually entered in LABVIEW at the beginning of each run. Model numbers and specifications of all data acquisition apparatus are provided in Appendix A.

Chapter 4 - Experimental Procedures

4.1 Calibration

4.1.1 Load Cell Unit (LCU)

The LCU required manual calibrations with known weights to determine the individual load cell responses. Forces and moments were isolated into each of the primary directions while recording the resulting voltages of the eight load cells. A single cable applied F_x (drag force) and F_y (side force) to the model, and weights placed directly on top of the model provided F_z (lift force). A single cable pulling in either the x- or y-direction with a known moment arm (height above the LCU centroid) applied M_y (pitch moment) or M_x (roll moment), respectively. Two cables connecting at opposite sides of the model and pulling in opposite directions applied M_z (yaw moment). All forces and moments were calibrated in the positive and negative directions with the exception of the F_z . In this case, mechanical limitations prevented pulling upwards and calibrating in the negative z-direction.

During calibration, the turret and its instrumentation apparatus were in precisely the same configuration as during testing. Any stiffness added by wires and tubes running from the inside of the turret to the instrumentation cavity was taken into account by calibration about all three axes. This stiffness was minimized by placing slack in all wires and connecting the stainless steel pressure tap tubing to flexible Tygon tubing shortly after entering the instrumentation cavity. Such added stiffness would most likely be non-linear, and non-linear effects were not noted in any of the calibration curves. In addition,

calibrations in each positive and negative direction produced lines with slopes nearly identical in magnitude for the primary load cells under consideration.

For each calibration, a zero point (no weight applied) was taken first, followed by intervals of increased weights until the maximum calibration load was reached. After the maximum load, weights were decreased in the same intervals until a second zero point was taken. Hysteresis in the cable/pulley system was avoided by lifting the weight stack at each calibration point (both while ascending and descending in weight) until the cable barely began to sag. The weight stack was then slowly lowered into place at approximately the same rate for each data point. Examination of the calibration curves in Figures 42 through 60 verifies the absence of any noticeable hysteresis.

These loadings produced the primary and secondary calibration curves, the latter of which indicated the coupling of the load cells under each loading condition. The slopes of the linear calibration curves were calculated from a least squares fit to the data. All primary calibration curves had a correlation coefficient of at least 0.9999. Once the slopes had been determined, a calibration matrix was formed according to

$$\{EC\} = [A] \{F\}$$

in which $\{EC\}$ was the 6x1 measured voltage vector, $[A]$ was the 6x6 coefficient matrix containing the calibration curve slopes, and $\{F\}$ was the 6x1 applied load vector. During the testing phase, the forces and moments acting on the model were calculated by multiplying the measured voltage vector by the inverse of the calibration matrix.

4.1.2 Pressure Systems Inc. (PSI) System

A set of LABVIEW commands directed the PSI system to perform a self-calibration at the beginning of each set of runs. Once started, the stand-alone PSI system would apply a series of known pressures to the electronic pressure scanner and isolate each pressure tap in turn. The result was a set of calibration curves that was used to calculate the pressures in the eleven static taps on subsequent runs.

4.2 Testing

Five separate configurations were tested during this study: clean turret, small or large splitter plate attached, and small or large fairing attached. For each of the four latter configurations, data were taken at 0° , $\pm 2.5^\circ$, and $\pm 5^\circ$ sideslip angles, but the clean turret was tested at 0° each time. When the model was rotated, the LCU rotated as well, so all data were taken with respect to the model coordinate axes. Each data run consisted of nine tunnel speeds, as determined from the tunnel dynamic pressure. The dynamic pressure ranged from one inch of water (equivalent to 20 m/s) to nine inches (65 m/s) in one-inch increments. The maximum speed tested corresponded to a Mach number of 0.19. The forces and pressures acting on the model were zeroed before beginning each data run and checked at the end of each run to catch any shift in data, but no hysteresis effects were encountered during testing.

At each speed, 2000 samples were taken from the LCU and PSI system at a scan rate of 2024 samples per second. Those samples were then averaged into one data point and saved. Ten such data points were taken at each given speed, after which the tunnel

velocity was increased and another set of data points was taken. During testing, load cell forces were monitored to ensure that the structural limits of the load cells were not exceeded. The turret and any attached splitter plate or fairing were visually monitored as well to prevent vibrations from developing and damaging any of the testing apparatus.

4.3 Flow Visualization

4.3.1 Tufts

The turret, both fairings, and the small splitter plate were extensively tufted for this phase of the study. Embroidery thread 0.8-mm (1/32-in) thick was cut into 1.3-cm (1/2-in) lengths and placed on the model in a closely spaced grid pattern. Tufts of this size were useful in identifying separation regions, the strength of separated flow, and dominant flow frequencies. However, as discussed in Section 6.5.1, the tufts did induce a small amount of flow field interference. A lack of optimal viewing windows on one side of the tunnel dictated that tufts be placed predominantly on the opposite side of the model. Several tufts were placed on the poor visibility side of the model to ensure flow symmetry, but these tufts were not photographed. The mahogany turret and the aluminum splitter plate were both dark in color, and bright yellow tufts were applied to both to enhance visibility. The fairings were painted yellow, however, and dark gray tufts were applied for the same reason. Once the thread was cut into individual tuft lengths, each tuft was applied using a triangular piece of fiber tape. A drop of quick-drying glue was placed onto the free end of each tuft to prevent fraying when the tufts were subjected to the rapid unsteady motions of the flow in the wind tunnel.

Still photographs and high-speed video were taken of the various tufted configurations. Three discrete tunnel speeds were used for each configuration: 37, 46, and 55 m/s (120, 150, and 180 ft/s). For each tunnel speed, one still photograph was taken of the overall configuration with slight emphasis on the area near the junction of the turret and the fairing/splitter plate. Approximately five 5-second high-speed video segments (200 frames/second) were recorded at each speed as well. The video segments provided emphasis on the following areas: overall shot of turret and fairing/splitter plate, close-up of top junction of turret and fairing/splitter plate, close-up of middle junction, close-up of lower junction, and close-up of fairing or splitter plate.

4.3.2 Oil Flow

Oil flows were used to identify the smaller-scale flows around the clean turret and test the effects of opening and closing the gap above the instrumentation cavity. Prior to this phase, the turret and surrounding area on the ground plane were painted flat black to give the greatest contrast to the white oil. A blend of Rosco Fluid (used in fog-makers) and titanium dioxide (for white pigment) was applied to the turret in hundreds of tiny flecks by "snapping" the bristles of a small brush held several inches from the turret. While the turret was still wet, the tunnel speed was brought up to 55 m/s (180 ft/s) and the drops were spread in the direction of the flow around the turret. When a steady-state condition was reached, the tunnel was turned off and pictures were taken of the oil streamlines on the turret. This method yielded the sharp, descriptive flow images in Chapter 6 and has traditionally been shown to yield very good information about the flow on a body surface (Yang, 1989: 93). Figure 13 shows the turret before any wind had been

applied, and the various images in Section 6.1 show the oil after it had reached a steady-state condition at a tunnel speed of 55 m/s (180 ft/s).

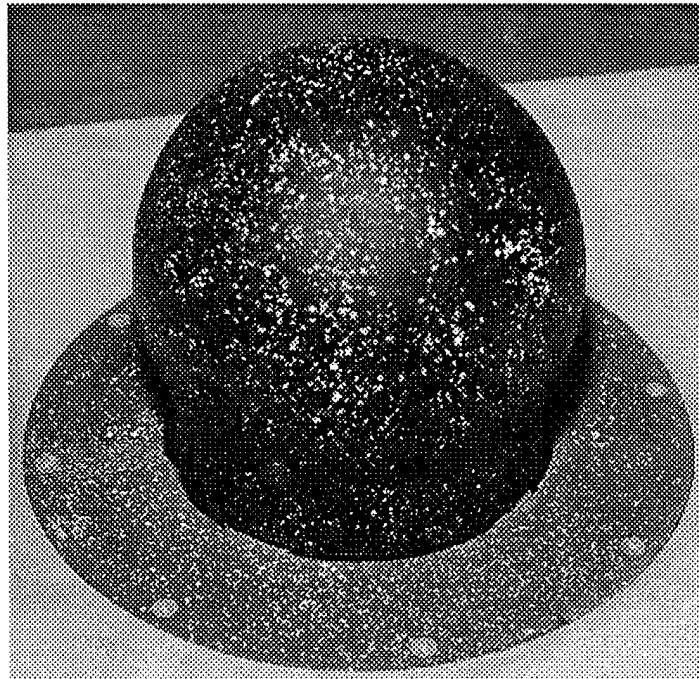


Figure 13. Oil applied to turret, wind off

Chapter 5 - Data Reduction

The raw data files produced by LABVIEW were reduced into the various force and pressure coefficients by a MATLAB routine. All output data in the AFIT 1.5-m (5-ft) wind tunnel were given in English units. These units were carried throughout the data reduction process for consistency, and the conversion to any necessary metric units was postponed until after the final quantities were calculated. This chapter outlines the calculations behind the two main products of this study, the drag coefficient and the pressure coefficient.

5.1 Drag Coefficient

The non-dimensional drag coefficient, C_D , was calculated from the definition

$$C_D = \frac{D}{\frac{1}{2} \rho \cdot V^2 \cdot S} \quad (1)$$

where:

D:	Drag force	[lb _f]
ρ :	Air density	[slug/ft ³]
V:	Tunnel velocity	[ft/s]
S:	Turret frontal area	[ft ²]

Note that the equivalent unit relation $\left(1 \text{ slug} = 1 \frac{\text{lb}_f \cdot \text{s}^2}{\text{ft}} \right)$ made the above definition

dimensionless. Each of the four quantities in Equation (1) will be discussed in the following sections.

5.1.1 Drag Force, D

As described in Appendix B, the raw voltages from the eight load cells were transformed into six combined voltages, EC_1 through EC_6 , corresponding to the three forces and three moments acting on the turret model. The calibration coefficient matrix $[A]$ was determined such that

$$[A]\{F\} = \{EC\} \quad (2)$$

in which $\{F\}$ was the 6x1 force/moment vector and $\{EC\}$ was the set of six combined voltages. Given the combined voltages for a "data point", the applied forces were calculated using

$$\{F\} = [A]^{-1}\{EC\} \quad (3)$$

The drag force, D, was the first element of F and was in units of lb_f .

5.1.2 Air Density, ρ

The air density was calculated from the ideal gas law

$$\rho = \frac{P}{R \cdot T} \quad (4)$$

where:

P:	Atmospheric pressure	$[lb_f/ft^2]$
R:	Specific gas constant	$[1716.2 \text{ ft}^2/s^2 \cdot ^\circ R]$
T:	Air temperature	$[^\circ R]$

Using the equivalent unit relation in Section 5.1 gave ρ in the desired units, $slug/ft^3$.

The barometric pressure in Building 19 was measured with a mercury barometer and was given in units of inches of mercury (" Hg). To convert this pressure to lb_f/ft^2 , the following conversion factor was used:

$$30 \text{ "Hg} = 1 \text{ atm} = 14.696 \text{ lb}_f/\text{in}^2 = 2116.2 \text{ lb}_f/\text{ft}^2$$

The temperature readout from the tunnel thermocouple was given in $^{\circ}\text{F}$, and the conversion to $^{\circ}\text{R}$ was

$$T(^{\circ}\text{R}) = T(^{\circ}\text{F}) + 459.69$$

5.1.3 Tunnel Velocity, V

The tunnel velocity was calculated directly from Bernoulli's Law. Note that the stagnation (total) pressure of the AFIT 1.5-m (5-ft) wind tunnel is atmospheric pressure.

$$P_{total} = P_{atm} = P_{tun} + \frac{1}{2} \rho V^2 \quad (5)$$

or

$$V = \sqrt{\frac{2}{\rho} (P_{atm} - P_{tun})} \quad (6)$$

The pressure difference $(P_{atm} - P_{tun})$ was read directly from the differential pressure transducer that monitored the pressure at the entrance to the tunnel test section. Since this quantity was given in inches of water (" H_2O), another conversion factor was used to convert to lb_f/ft^2 :

$$407.2 \text{ "H}_2\text{O} = 1 \text{ atm} = 14.696 \text{ lb}_f/\text{in}^2 = 2116.2 \text{ lb}_f/\text{ft}^2$$

The air density, ρ , was the same quantity as described in Section 5.1.2 and was in units of slug/ft³. Once again, the equivalent unit relation given in Section 5.1 converted the units of air density, and the resulting tunnel velocity was given in ft/s.

After the tunnel velocity had been determined, a test section blockage factor was applied to adjust for all objects placed in the test section (Rae and Pope, 1984: 371). For an unusual shape in a test section, the correction factor was given by

$$\varepsilon_t = \frac{1}{4} \frac{\text{Model frontal area}}{\text{Test section area}} \quad (7)$$

The combined area of the ground plane, instrumentation cavity, and turret model was 1.161 ft², and the test section area was 19.63 ft². This gave a blockage correction of

$$\varepsilon_t = \frac{1}{4} \left(\frac{1.161 \text{ ft}^2}{19.63 \text{ ft}^2} \right) = 0.0148 \quad (8)$$

The equivalent blockage in the wind tunnel test section was less than 2%, and the corrected wind tunnel velocity, V_{corr} , was

$$V_{\text{corr}} = V(1 + \varepsilon_t) = V(1 + 0.0148) \quad (9)$$

5.1.4 Turret Frontal Area, S

The drag coefficient for the turret was referenced to the turret frontal area, given in ft². This area was calculated from a computer drawing of the full-scale turret (subsequently reduced to half-scale) which was also used to machine the turret model. The turret model frontal area was 0.485 ft².

5.2 Pressure Coefficient

The non-dimensional pressure coefficient, C_p , was calculated from the definition

$$C_p = \frac{P_{local} - P_{atm}}{\frac{1}{2} \rho \cdot V^2} \quad (10)$$

where:

P_{local} :	Local pressure on turret surface	[lb _f /ft ²]
P_{atm} :	Atmospheric pressure	[lb _f /ft ²]
ρ :	Air density	[slug/ft ³]
V :	Tunnel velocity	[ft/s]

The equivalent unit relation made the above definition dimensionless as in the case of the drag coefficient.

The quantity $(P_{local} - P_{atm})$ was output directly from the PSI system for each of the eleven pressure taps. Since this pressure difference was given in inches of water, the conversion factors given in Section 5.1.3 were used again.

The dynamic pressure in the denominator of the pressure coefficient was determined in the same way as for the drag coefficient.

Chapter 6 - Results and Discussion

Quantitative data collected in this study consisted of forces and pressures acting on the turret model. These data were necessary to quantify the changes in drag, pressure distribution, and stability characteristics when fairings and splitter plates were added to the turret, but the data did not always provide an explanation of the reasons why these changes were taking place. Flow visualization was the key to this phase of the study, and several flow visualization methods were used to give an accurate description of the complicated flow field surrounding the turret model.

The discussion begins with a description of the observed flow field for each of the configurations, followed by the pressure distribution and drag results. Stability properties of the fairings and splitter plates follow the drag results. The final four sections discuss the use of trip strips, sealing of the instrumentation cavity, results from the dynamic response pressure transducers, and error analysis.

6.1 Flow Field Description

6.1.1 Clean Turret

The flow at the front of the unmodified (clean) turret is shown in Figure 14. This oil flow was produced at 55 m/s (180 ft/s) for a duration of approximately one minute. The larger stationary oil drops in Figure 14 indicated the stagnation region at the front of the turret. Miniscule stationary oil drops were scattered over the entire turret surface, but these did not indicate a stagnation condition; the tiny drops simply did not contain

sufficient oil to allow motion along the turret surface. The oil streaks that originated at the edges of the stagnation region indicated the direction of the flow as it was forced over and around the turret. A small amount of reverse (upstream) flow can be seen on the ground plane near the front of the turret, and the remaining flow on the ground plane was directed around and away from the base of the turret.

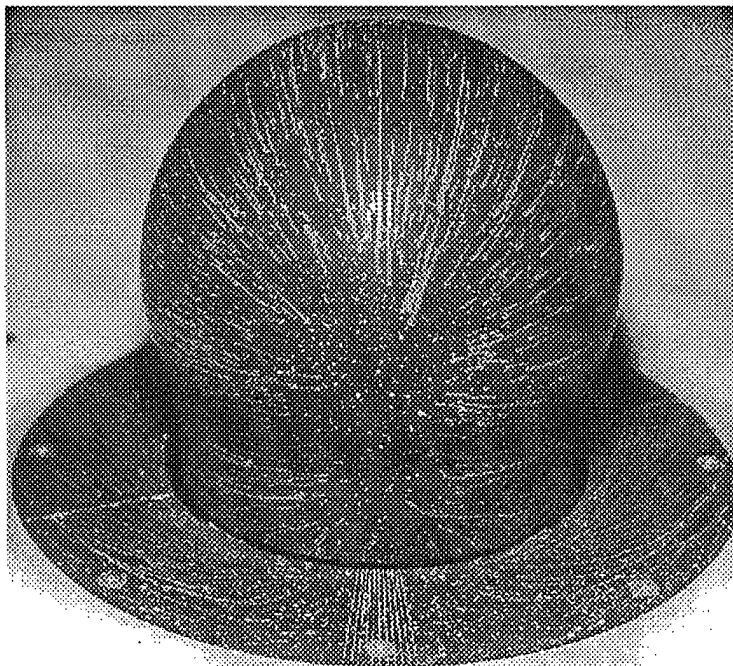


Figure 14. Oil flow, 55 m/s (180 ft/s), front view of turret

The flow near the base of the turret can be visualized as a horseshoe vortex that forms at the front of the turret and extends around the sides and far downstream (see Figure 15). Horseshoe vortices commonly develop near the junction between a body and

a wall (Belik, 1973:48). Further, Figure 16 shows a physical model of the horseshoe vortex that forms around the base of a finite circular cylinder placed on a flat plate.

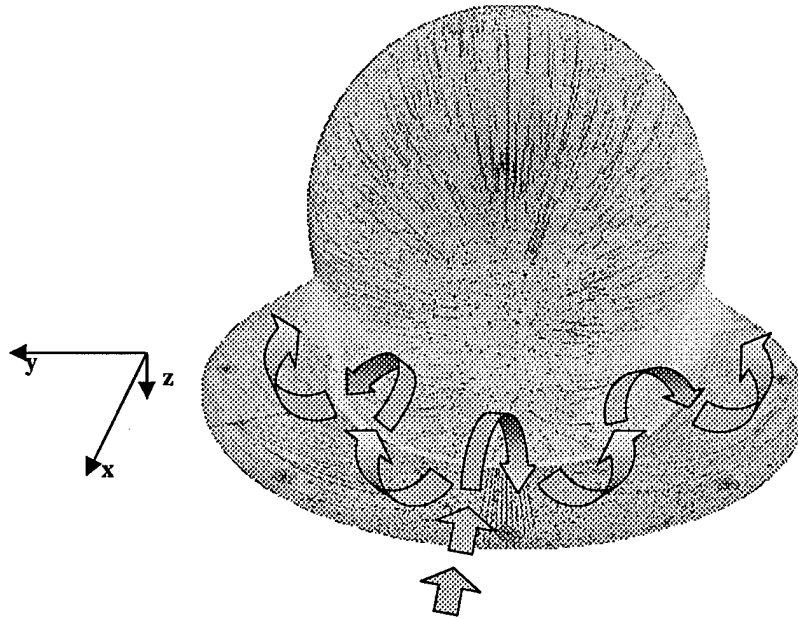


Figure 15. Horseshoe vortex representation, front view of turret

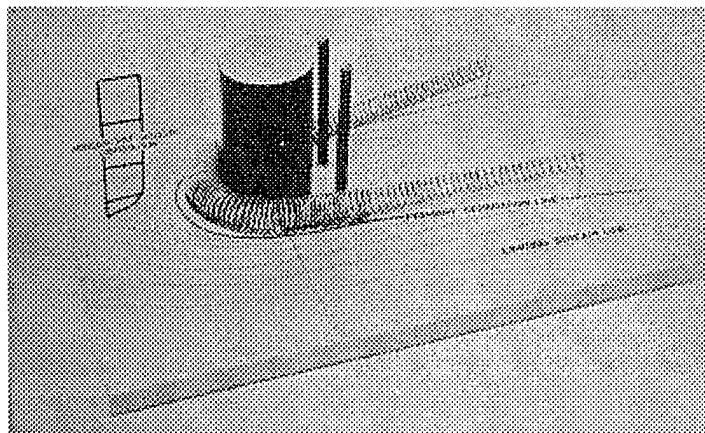


Figure 16. Horseshoe vortex model (Belik, 1973:47)

In this study, as the flow neared the area on the turret where the spherical portion was blended to the cylindrical base, the flow was turned downward and began to form a vortex rotating about the y-axis. A combination of the turret geometry and the velocity profile in the boundary layer of the ground plane (high velocity at the upper edge of the boundary layer and zero velocity at the ground plane) caused the flow to begin its downward rotation. When the flow reached the front of the turret, the higher-energy air near the upper edge of the boundary layer sought the path of least resistance and moved to the lower-energy air near the ground plane. Viewed over time, this process generated a vortex near the base of the turret rotating about the y-axis.

The Blasius solution predicted a turbulent boundary layer thickness of 1.9 cm (0.75 in) at the front of the turret, and this was approximately the height at which downward flow appeared on the turret in Figure 14. The developing vortex then split into two separate vortices that traveled around the sides of the turret while continuing to rotate as shown. The direction of rotation caused stagnation on the turret near the top of the vortex and an upward velocity component above the vortex as shown in the side view of the oil flow in Figure 17. This figure also shows stagnated flow in small separated regions on the ground plane and turret base beginning at approximately 90° from the front of the turret.

The main separation zone occurred at the rear of the turret as shown by the oil flow in Figure 18 and the tuft photo in Figure 19. The oil flow also captured the reverse flow on the ground plane in the wake of the turret. Although the oil flow seems to indicate a well-behaved separation bubble behind the turret, high-speed video of the tufts and

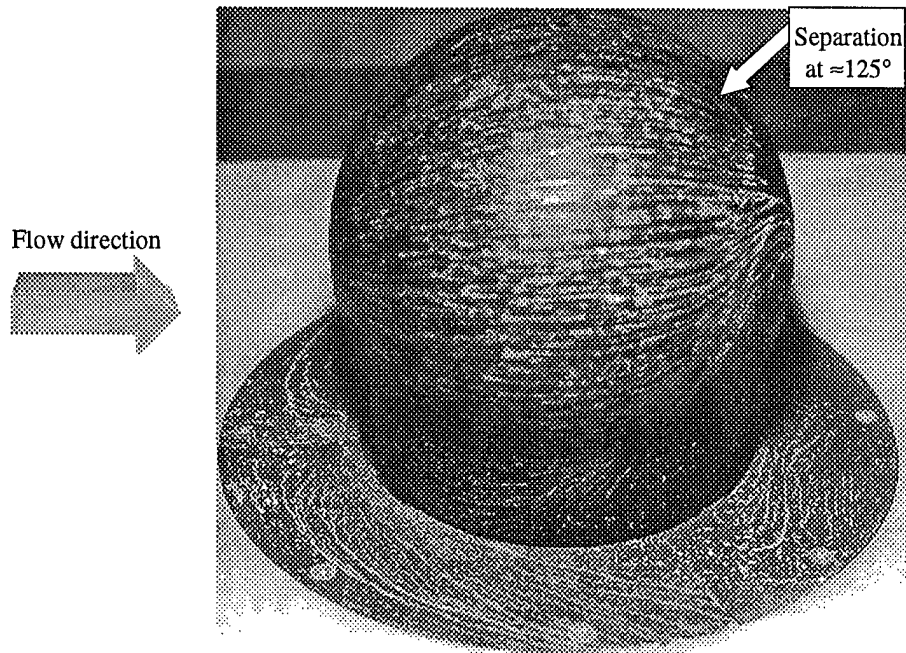


Figure 17. Oil flow, 55 m/s (180 ft/s), side view of turret

qualitative “tuft-on-a-wire” tests portrayed a highly chaotic region of three-dimensional vortices. In addition to the vortex street shed from the sides of the turret (similar to those encountered behind a circular cylinder), high-intensity vortices were shed from the top of the turret. This strong flow over the top of the turret became evident when testing the splitter plates and is addressed further in Section 6.1.2. Gravity acting on a large quantity of oil in the separation zone caused the large vertical streaks to appear in Figure 18; these should not be regarded as an indication of the flow in that region. Similarly, the majority of oil streaks near the top mounting hole in Figures 17 and 18 were pulled downward by gravity; tuft observations indicated separation near 125° ($\pm 5^\circ$ -- see Appendix C) which is 10° - 15° forward of the point where the oil flow stopped (see Figure 19).

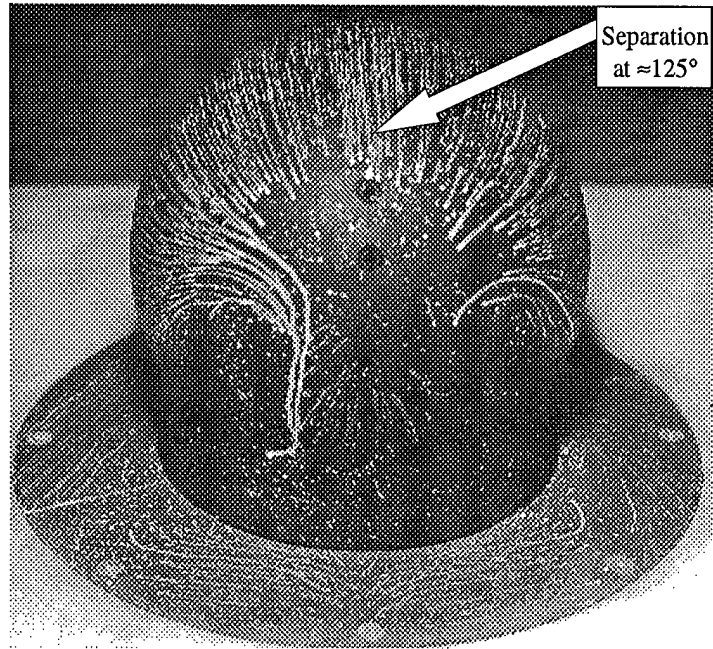


Figure 18. Oil flow, 55 m/s (180 ft/s), rear view of turret

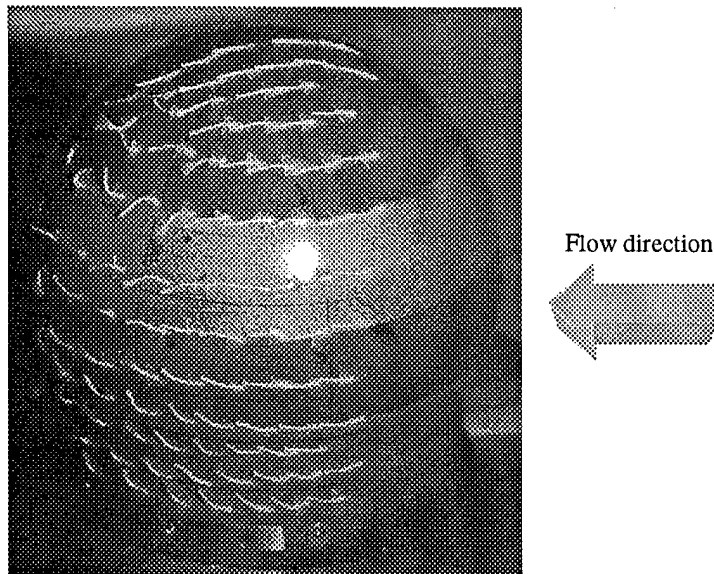


Figure 19. Tuft run, 55 m/s (180 ft/s), side view of turret

The photographs and high-speed video of the tufts gave dynamic descriptions of the flow near the surface of the turret. As shown in Figure 19, the flow remained attached through approximately 120° aft of the leading edge. Blurred tufts near and beyond the 125° meridian were oscillating rapidly and indicated that the flow had become separated. Tufts placed along the top of the turret separated near 125° from the front as well. In the separated region, tufts generally oscillated between frequencies of 20-50 Hz. Near the base of the turret, Figure 19 captures the upward motion of the flow above the horseshoe vortices and is in close agreement with the oil flow in Figure 17.

6.1.2 Splitter Plates

Tuft photos were taken of the turret with only one of the splitter plates (the small one); minimal differences in drag and pressure distributions between the small and large splitter plates indicated little variation in the flow field when either was attached to the turret. Tuft motion indicated that the splitter plates did not alter the separation point on the turret by any noticeable amount. Their primary function was to reduce the motion of the vortex street in the wake of the turret, and at least partial success was apparent from the drag reduction each splitter plate caused. However, as will be discussed in the following sections, the drag reduction was not as significant as previous studies have demonstrated. The key to this discrepancy is found in the tuft behavior in Figure 20.

With the splitter plate attached, the tuft motion on the turret itself closely resembled that seen on the clean turret, and the tufts indicated separation at approximately 125° . However, at the base of the turret, three tufts bent completely backward demonstrated

strong reverse flow near the ground plane. The tufts located on the upstream portion of the splitter plate were in a strong separation zone and were turned sharply upwards or downwards depending on their position on the splitter plate. Since the splitter plate reduced the strength of the vortex street shed from the sides of the turret, the flow over the top of the turret became increasingly dominant and easier to visualize.

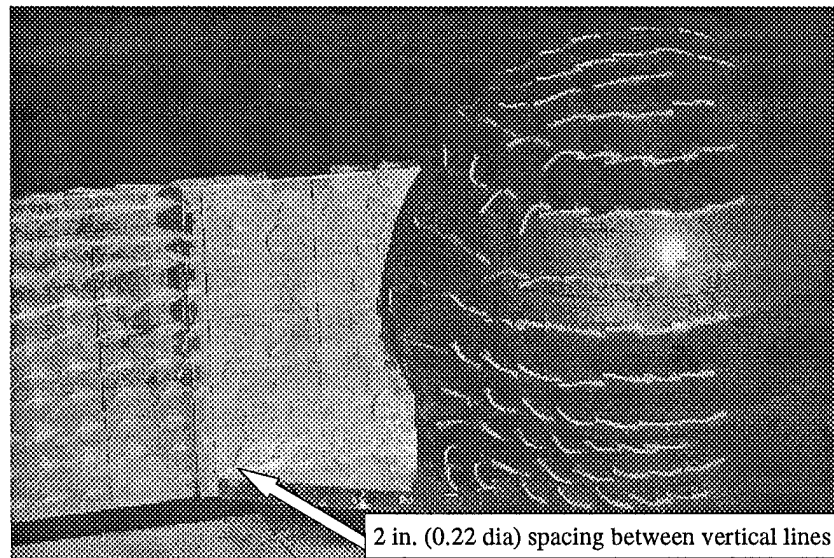


Figure 20. Tuft run, 55 m/s (180 ft/s), small splitter plate installed

Figure 20 is the strongest indication of the dominant top vortices that shed from the top of the turret and rotated about the y-axis, much like the initial rotation of the horseshoe vortex. Although only partially shown in the above figure, the tufts indicated a consistent downward motion for 1 diameter aft of the splitter plate/fairing junction. The remaining tufts did not show a dominant flow direction but simply oscillated about

horizontal lines drawn on the splitter plate. This verified that the splitter plate did not prevent separation; it was able to reduce the motion of the vortices shed from the sides of the turret but could not prevent the dominant top vortices from developing behind the turret. As the top vortices descended on either side of the splitter plate, they created a low-pressure zone similar to that of the clean configuration. The splitter plate was therefore ineffective in reducing the size of the low-pressure wake behind the turret.

6.1.3 Fairings

The flows around the turret with the small and large fairings installed are shown in Figures 21 and 22, respectively. The most striking feature of Figure 21 is the relatively large separation zone located upstream and downstream of the fairing attachment point. Although the small fairing provided a streamlined shape for the flow to attach onto behind the turret, the flow remained separated for approximately 1.3 diameters along the fairing. This occurred because the small fairing was located well within the separated wake of the turret, and the flow developed high levels of vorticity before reaching the fairing surface. Although the drag reduction (presented in Section 6.3.3) was appreciable, the large separated region near the fairing attachment point resulted in poor flow quality in that area. The tufts in that separated region gave an additional indication of the strong vortices shedding from the top of the turret. Near the top of the fairing, several rows of tufts showed strong reverse flow, while the tufts on the lower half of the fairing displayed a sharp downward flow velocity. Separation appeared along the top and sides of the turret (with small fairing attached) at approximately the same points as on the clean turret, 125° behind the leading edge.

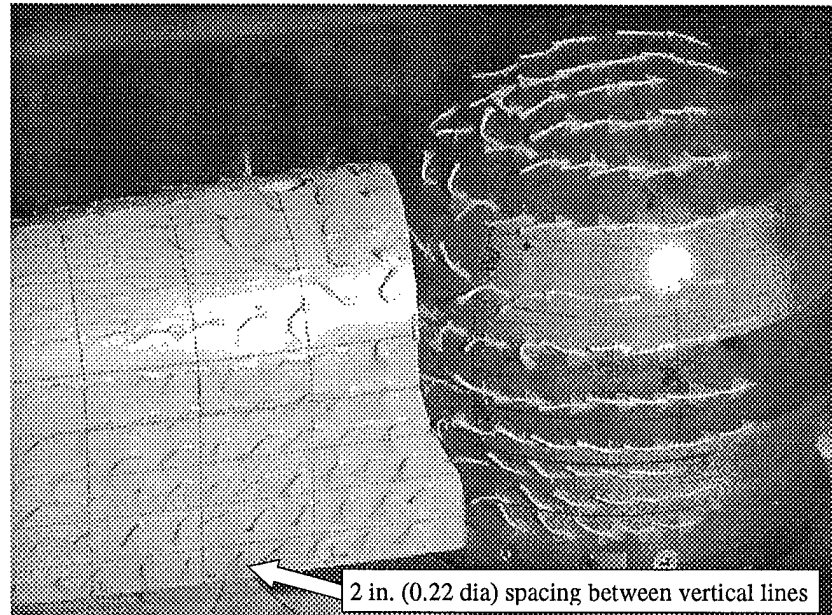


Figure 21. Tuft run, 55 m/s (180 ft/s), small fairing installed

When the large fairing was installed, the separation region near the fairing attachment point was nearly eliminated, as shown in Figure 22. Flow along the side of the turret showed slight separation near the last column of tufts placed on the turret (approximately 135° from the turret leading edge). This separation region was extremely small, however, and in most cases the flow reattached upon reaching the second column of tufts placed on the fairing. An area of downward velocity occurred near the fairing/turret junction and the base of the fairing, but this area was much smaller and weaker than that of the small fairing. The main reason for this vast improvement in flow quality over the small fairing was the reduction in strength of the vortices shed from the top of the turret. Figure 22 shows the height of the large fairing extending nearly to the

top of the turret. Consequently, the top flow over the turret remained attached for the entire length of the turret and fairing. With the top flow completely attached and the side flow attached for all but approximately 0.2 diameters aft of the junction, the flow field created by this configuration was extremely well-behaved, and considerable drag savings resulted. A quantitative discussion of all drag results can be found in Section 6.3.

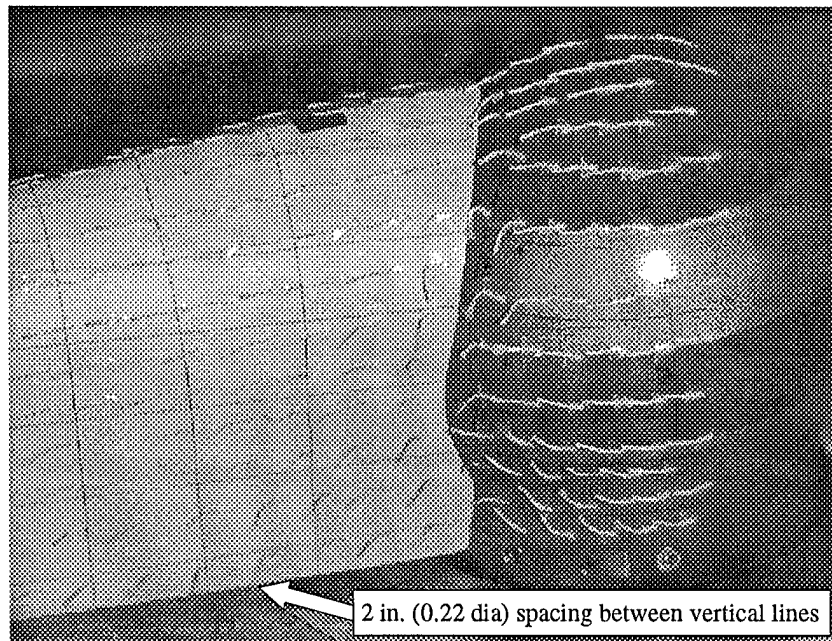


Figure 22. Tuft run, 55 m/s (180 ft/s), large fairing installed

6.2 Pressure Distribution

6.2.1 Clean Turret

The pressure distributions along the top and sides of the clean turret are plotted in Figure 23 against experimental distributions for a sphere and an infinite cylinder tested in previous studies. Since the flow over the top of the turret encountered the same hemispherical shape as the flow over the top of a sphere, the turret and sphere pressure distributions have very similar curves. With the base of the turret connected to the ground plane, however, the curves suggest that the mass flow of air forced around the top and sides of the turret was greater than the mass flow around the corresponding areas of a

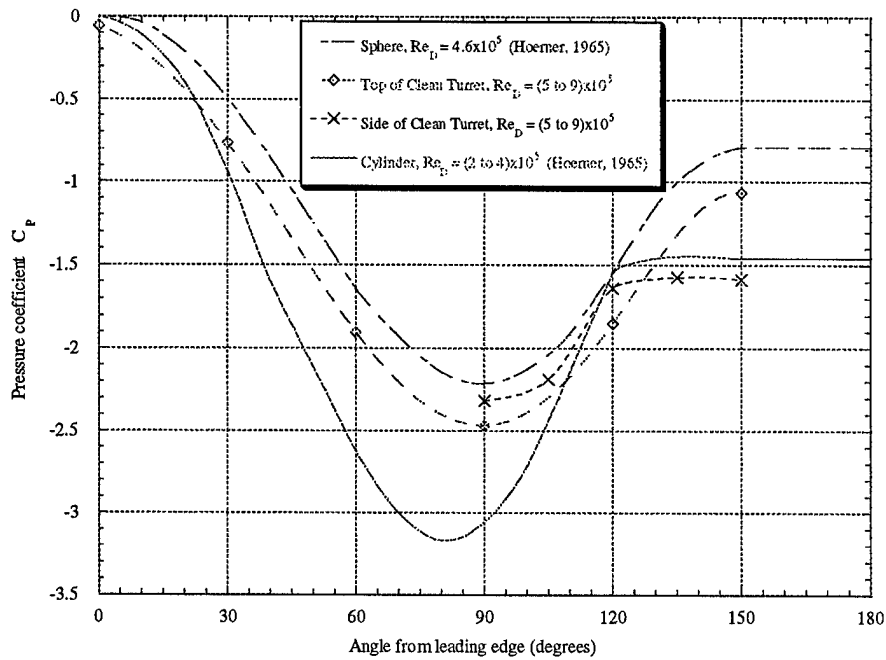


Figure 23. Pressure distribution, similar shapes

sphere at a given Reynolds number. This basic principle of continuity caused higher velocities and lower pressures in these areas of the turret as shown in the previous figure.

The pressure distribution around the side of the turret closely followed the sphere distribution in the range of 90° to 120° behind the front of the turret. However, after 120° the pressure distribution became nearly constant, and the flow had separated from the sides of the turret. Separation occurred on the infinite cylinder at the same point and gave another verification that the turret geometry could be considered a blend between a sphere and a cylinder. The pressure distribution along the side also verified the visual estimation of separation from tuft and oil flow pictures in section 6.1.1. Unfortunately, a lack of pressure taps along the top of the turret between 120° and 150° made estimation of the top separation point much more difficult. Separation over the sphere occurred near 150° , and at first glance the pressure distribution over the top of the turret seemed to indicate the same separation point. However, tuft and oil flows (Figures 17 through 19) have shown separation to occur near 125° along the top of the turret. The data would suggest that pressure taps added between 120° and 150° would read the same pressure as the 150° tap. These pressures would flatten out the pressure coefficient curve and move the top separation point near 125° , the point observed in the flow visualization studies.

6.2.2 Splitter Plates

Figures 24 and 25 show the pressure distributions around the turret with the small and large splitter plates installed, respectively. When the small splitter plate was attached,

it covered the last pressure tap along the top (150°), and the large splitter plate covered the last two pressure taps along the top (120° and 150°). In both cases, the splitter plates moved the side separation point slightly forward of the 125° point noted on the clean turret. This result was not verified by the tuft photos, for the change was within the $\pm 5^\circ$ error band inherent in the tuft measurements. The pressures along the top of the turret showed larger changes, however. From 90° aft of the leading edge and beyond, the pressures on the turret (with the splitter plates installed) were roughly 8% higher than the pressures on the clean turret. Since the splitter plates reduced the motion of the vortex street in the turret's wake, the vortices behind the turret were weakened and the flow over the top of the turret experienced more pressure recovery.

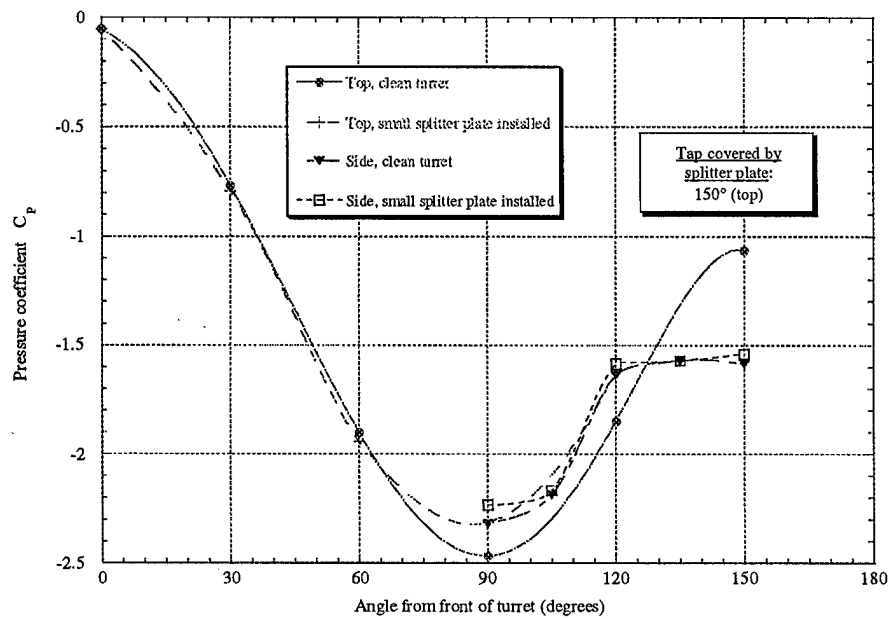


Figure 24. Pressure distribution, small splitter plate installed

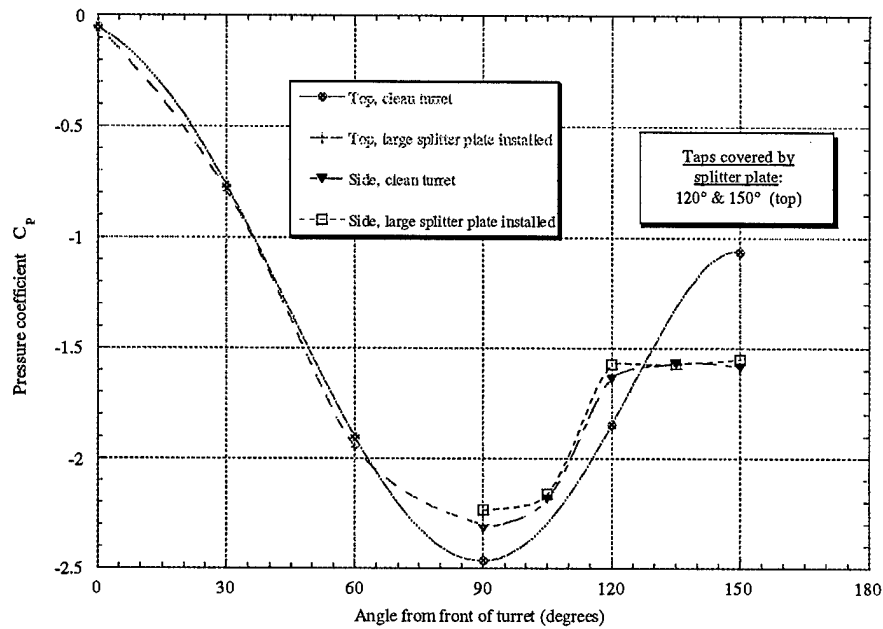


Figure 25. Pressure distribution, large splitter plate installed

6.2.3 Fairings

The pressure distributions around the turret with the small and large fairings installed are shown in Figures 26 and 27, respectively. Similar to the splitter plates, the small fairing covered the last pressure tap along the top (150°), and the large fairing covered the last two pressure taps along the top (120° and 150°). In addition, both fairings covered the last pressure tap along the side of the turret (150°). With the rear pressure taps covered by the fairings and no pressure taps in the fairings themselves, a complete description of the increased pressure recovery behind the turret cannot be given. Unlike the splitter plates, though, the fairings produced a significant pressure recovery along both the top and side exposed taps. The increased pressure recovery over the top

also suggested that the flow was slowing down before separating from the surface of the turret, and the trailing wake of vortices had been reduced in strength.

Figure 26 indicates that the small fairing delayed separation slightly along the side, and Figure 27 shows that separation did not even occur by 135° with the large fairing installed. The much smaller separation zone near the large fairing in Figure 22 verifies delayed separation, but the tufts in Figure 21 do not indicate any delayed separation with the small fairing attached. Since separation was delayed with the large fairing and the pressure data is significantly more accurate and quantitative, however, it is likely that separation was in fact delayed when the small fairing was installed. The resolution of the tufts was simply too coarse to verify this finding.

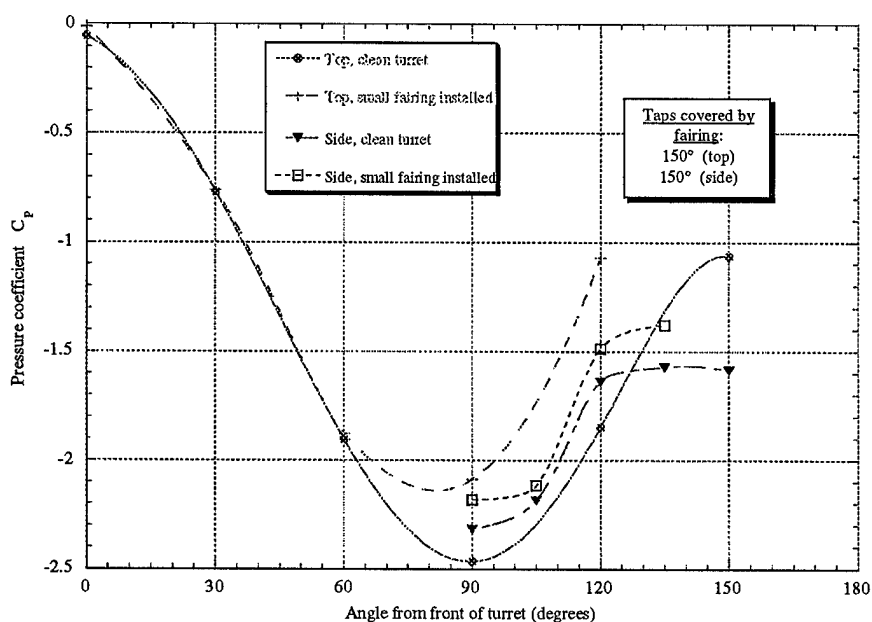


Figure 26. Pressure distribution, small fairing installed

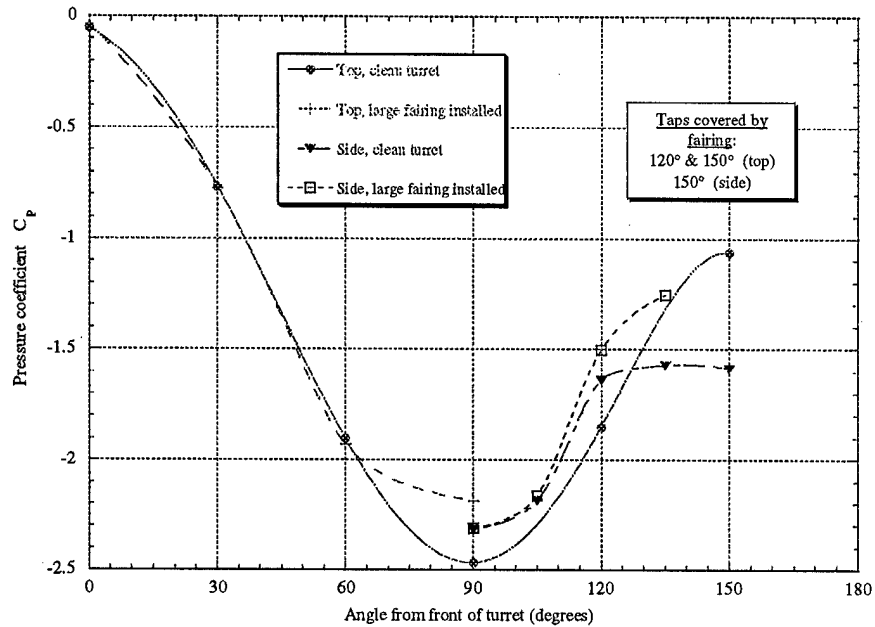


Figure 27. Pressure distribution, large fairing installed

6.3 Drag

6.3.1 Clean Turret

The measured drag coefficient for the clean turret is shown in Figure 28 in conjunction with related shapes tested in other studies. Although the turret was partially a sphere, the turret drag coefficient was nearly four times higher than a sphere at Re of 6×10^5 and higher. For a sphere, flow receives pressure relief from all sides, and the resulting separation region does not begin until approximately 155° from the leading edge around all sides (Hoerner, 1965:3-8). When the turret was attached to a wall (the ground plane), however, the base of the separation region behind the turret extended downward to the ground plane. This low-pressure wake was much larger than the corresponding wake behind a sphere and resulted in a large increase in pressure drag.

Figure 28 also shows that the turret drag coefficient was quite similar to a finite cylinder with a matching diameter to height ratio ($D/h \approx 1$) placed on a flat plate (a very similar configuration to the turret). The turret's slightly lower drag coefficient can be attributed to the streamlining near the top of the turret that is not present in the finite cylinder. Unfortunately, data for the finite cylinder was taken at a Reynolds number of approximately 1×10^5 and cannot be accurately extrapolated to the Reynolds number range in which the turret was tested. However, assuming the flow around the cylinder is still laminar at 1×10^5 , the cylinder is likely to experience a similar drag decrease in the general Reynolds number range as the other shapes. When this occurs, the flow

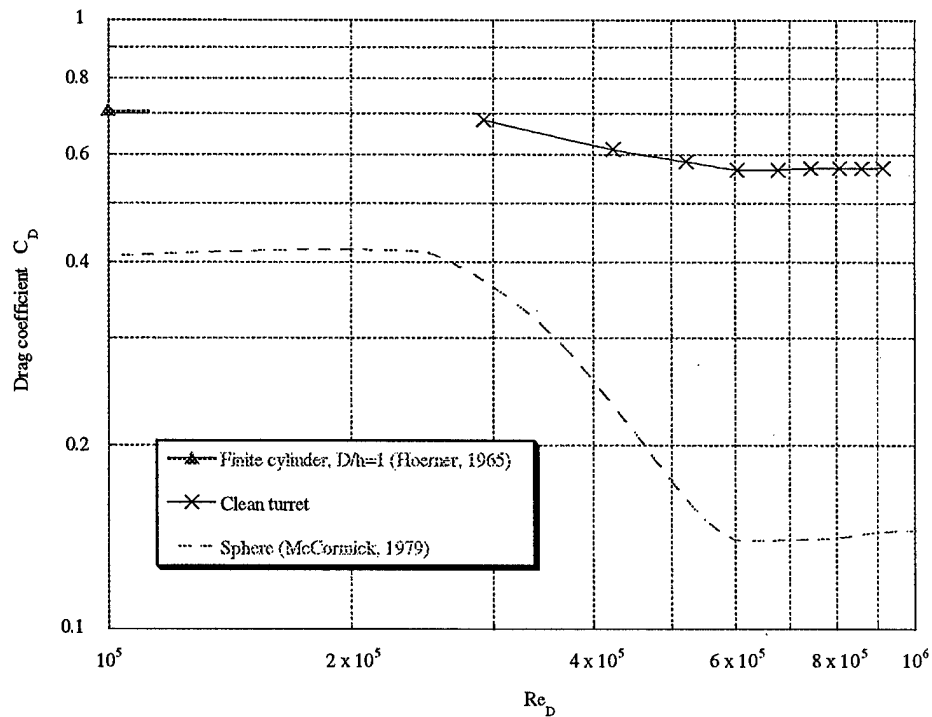


Figure 28. Drag coefficient comparison, similar shapes

transitions from laminar to turbulent and remains attached to the cylinder for a greater distance around the circumference. The separation region in the wake of the cylinder becomes smaller, drag decreases, and the cylinder drag coefficient would show a similar decrease as seen in Figure 28 for the clean turret.

6.3.2 Splitter Plates

As the theory in Chapter 2 predicted, the splitter plates were able to reduce the motion of the vortex street and produce a small reduction in drag. Figure 29 shows a 7% drag reduction for the small splitter plate and a 5% reduction for the large splitter plate. Contrary to intuition, the large splitter plate did not cause a greater drag reduction than the small splitter plate. Instead, the large splitter plate configuration produced a 2% increase in drag over the small splitter plate configuration.

A comparison of the splitter plates' pressure coefficient curves gave an explanation for the higher drag measured with the large splitter plate installed versus the small splitter plate configuration. With nearly identical pressure distributions around the top and side of the sphere, Figures 24 and 25 indicate that increasing the plate size beyond that of the small splitter plate did not gain any additional pressure recovery. Given the same amount of pressure recovery, the pressure drag for each splitter plate configuration was equal. Since the surface area of the large splitter plate was 1.7% greater, though, the large splitter plate configuration incurred an additional amount of skin friction drag.

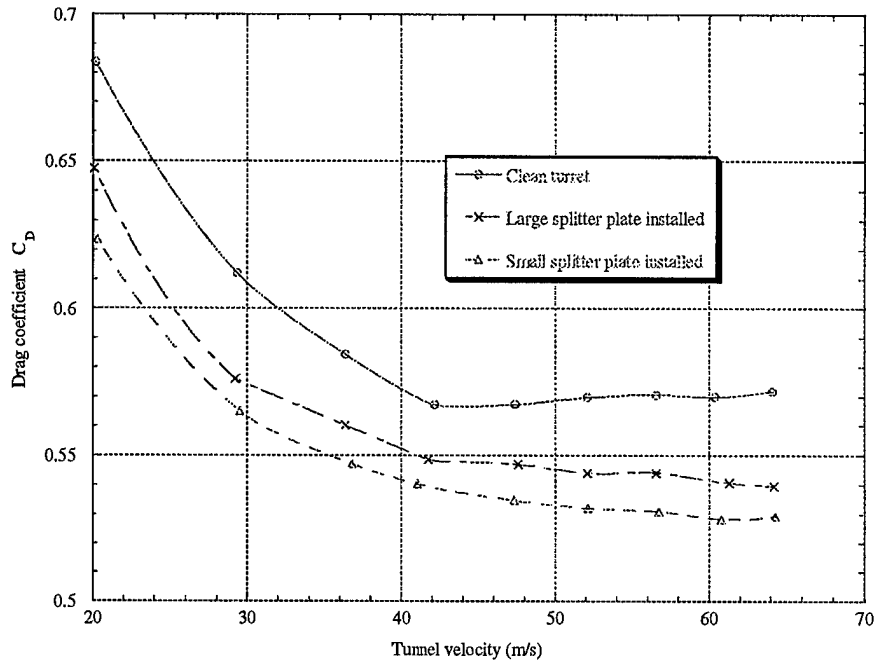


Figure 29. Drag coefficient comparison, splitter plates installed

The three-dimensional nature of the flow around the turret resulted in much poorer splitter plate performance than previous two-dimensional splitter plate studies have shown. For a cylinder spanning between two walls, a 4.2-diameter length splitter plate was able to reduce the drag by 43% at Reynolds numbers between 10^4 and 10^5 . For the same cylinder, an extremely short splitter plate (known as a Thwaites Flap) extended only $\frac{1}{4}$ of a diameter behind the cylinder but still reduced the drag by 15% (Hoerner, 1965:3-7). In this study, minimal 5-7% drag reductions resulted when the splitter plates were attached; they simply had no ability to eliminate the low-pressure zone created by the dominant vortices shedding from the top of the turret.

6.3.3 Fairings

Both fairings were highly successful in reducing the amount of drag measured for the clean turret, and the fairing results are shown in Figure 30 in conjunction with those of the splitter plates discussed previously. In contrast to the 7% and 5% drag savings with the small and large splitter plates, the installation of the small and large fairings resulted in drag reductions of 49% and 55%, respectively. Located in what would normally be the low-pressure wake behind the turret, the fairings prevented suction from acting on a large portion of the turret and reduced the pressure drag. Tuft behavior suggested that the position of the fairings also broke up the large-scale vortices in the wake and forced smaller, less-powerful vortices to form behind the turret instead. Finally, the streamlined

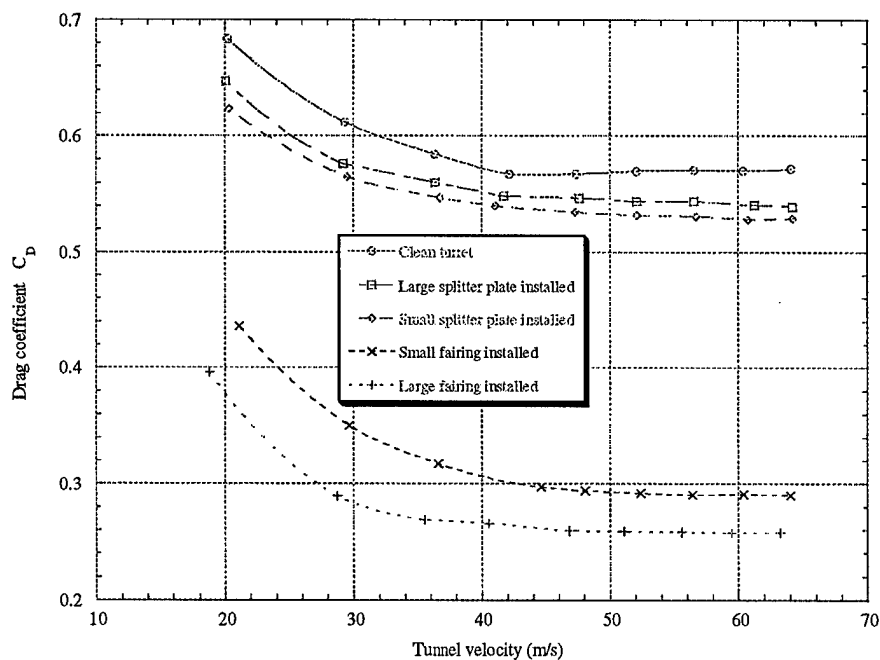


Figure 30. Drag coefficient comparison, fairings and splitter plates

shapes of the fairings reduced drag by delaying separation, inducing a greater pressure recovery, and allowing the flow to reattach behind the turret. Although the small fairing was too far within the separation region to eliminate the strong top vortices and cause reattachment, it was still able to achieve a drag reduction comparable to the large fairing by causing pressure recovery and preventing suction from acting on a portion of the turret. The greater success of the large fairing was a direct result of streamlining the top flow and creating attached flow over the vast majority of the turret/fairing surface. However, the larger surface area of the large fairing resulted in higher skin friction drag than the small fairing, which partially reduced the large fairing's overall success in reducing drag.

In a study on two-dimensional circular cylinders, a wedge-shaped aft fairing with a 2.1-diameter length (placed along the entire span of the cylinder) produced a 39% drag reduction at a Reynolds number of approximately 3×10^5 (Hoerner, 1965:13-19). The maximum thickness of the fairing was nearly the same as the cylinder diameter, but the simple wedge configuration was shorter and less streamlined than the large fairing/turret configuration in this study. This result highlights the success of using longer, more streamlined fairings (although not nearly as wide as the turret itself); even with three-dimensional effects, the fairings in this study created greater drag reductions than a two-dimensional wedge-shaped fairing as thick as the diameter of the cylinder it was placed behind.

6.4 Stability Properties

The stability properties of the large and small splitter plates and fairings are presented together in this section for ease of comparison. The main properties considered were the variations of the side force coefficient and yaw moment coefficient with sideslip angle, β . Refer to page xiii for a description of the axis and coefficient conventions used in this section.

The side force coefficients for each of the four drag reduction configurations are shown in Figure 31. For each configuration, a rotation into the wind resulted in a force proportional to the angle of rotation. The constant of proportionality varied between each

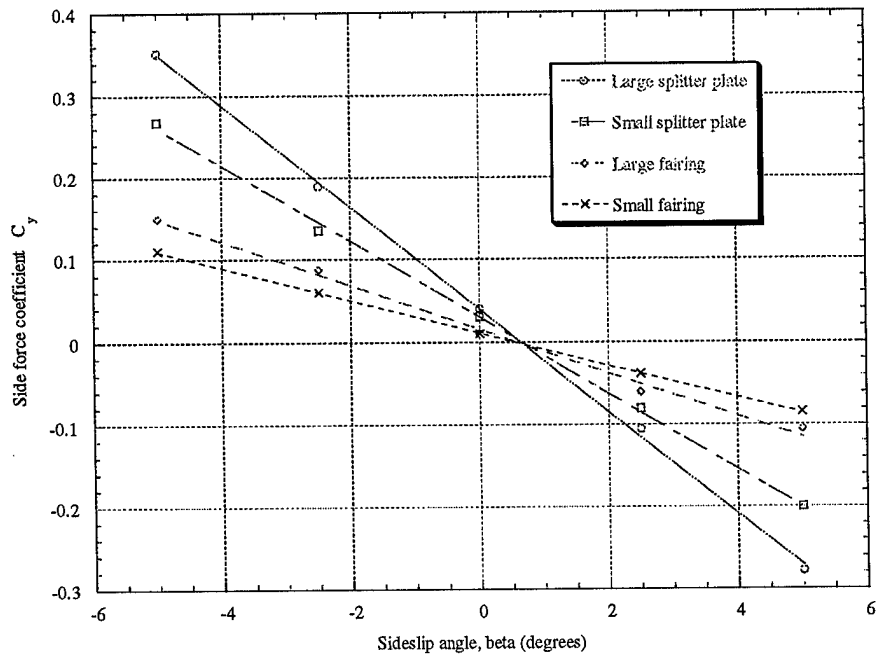


Figure 31. Side force coefficient comparison, fairings and splitter plates

configuration, but simple intuition could predict the general trends contained in Figure 31: the larger or less streamlined shapes produced higher side force coefficients at a given sideslip angle. Thus, the “worst” configuration (the one that produced the highest side forces) was the large splitter plate, followed by the small splitter plate, large fairing, and small fairing. Table 1 presents the slopes of each of the lines in Figure 31 and the approximate slopes of the yaw moment curves in Figure 32.

Table 1. Side force and yaw moment coefficient slopes (vs. β)

	Large splitter plate	Small splitter plate	Large fairing	Small fairing
$C_{y\beta}$	-0.062	-0.046	-0.026	-0.019
$C_{n\beta}$ (linear approx.)	0.47	0.32	-0.17	-0.18

The non-linear yaw moment results were not quite as intuitive as those for the side force coefficient, however. As the trailing edge of each fairing or splitter plate was rotated into the wind, the expected result was a restoring yaw moment that tended to “weathervane” the configuration parallel with the freestream. In stability terms, this would translate into a positive C_n vs β slope. In Figure 32, an apparent problem exists with the results for both fairings. The splitter plates had positive C_n vs β slopes, as expected, but the fairings had negative (destabilizing) C_n vs β slopes. Instead of aligning the fairing/turret configuration with the freestream, Figure 32 indicates that both fairings

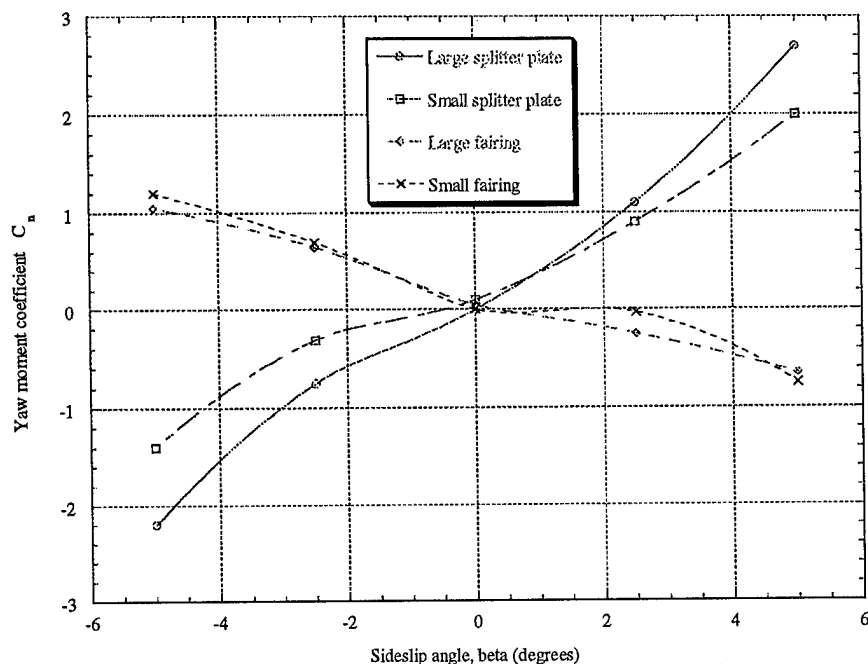


Figure 32. Yaw moment coefficient comparison, fairings and splitter plates

tended to rotate further into the wind when placed at a sideslip angle up to $\pm 5^\circ$. The stability data and tuft photos collected during this part of the study suggest that the destabilizing moments occurred as a result of the small sideslip angles tested. The following discussion highlights a possible cause for this phenomenon, but additional testing is needed to verify this or any other such cause.

At sideslip angles of 5° and less, no portion of the fairings was visible beyond the frontal profile of the turret, and the destabilizing yaw moments possibly occurred as a result of the fairings acting as lifting bodies (Emsley, 1998). The fairing cross-sections

were similar to the leading edge of an airfoil, and the flow was essentially aligned with the span of the airfoil. As the flow passed the turret, the flow impinging on the windward side of the rotated fairing was forced over and around the fairing to meet the flow passing the other side of the turret. Flow forced over the windward side of the fairing remained attached and moved faster than the flow expanding (and decelerating) in the larger leeward area behind the fairing. This produced a "lifting" force on the fairing that was directed partially upstream, creating a destabilizing yaw moment for the turret/fairing combination. This phenomenon did not occur with the splitter plates, though. Any flow forced over the top of the splitter plates shed from the sharp top edge and immediately separated.

If the fairings in this study were rotated further than 5° , however, they should have begun to resemble bluff bodies and "weathervane" toward smaller sideslip angles. Additional testing at larger sideslip angles should have produced the desired positive-sloped C_n vs β curves, but safety concerns in the AFIT 1.5-m (5-ft) wind tunnel prohibited testing at those angles. The fairing and splitter plate cantilevered mounting system was sensitive to lateral forces and twisting moments, and a maximum $\pm 5^\circ$ sideslip angle helped prevent the possibility of shearing a fairing or splitter plate from the turret and severely damaging the model or wind tunnel.

6.5 Effects of Testing Methods

6.5.1 Trip Strips

During the flow visualization phase, tufts had been placed almost exclusively along one side of the turret, fairings, and small splitter plate to facilitate viewing with still and high-speed video cameras. Once the first fairing was attached to the turret, however, a significant amount of flow asymmetry was noted behind the turret. Tufts along the top of the fairing indicated a strong flow from the clean side of the fairing to the tufted side. In this configuration, the tufts were introducing flow field interference and caused early separation on the tufted side of the turret. However, flow was staying attached to the clean side of the turret for a longer distance and possessed the additional momentum to cross the centerline of the fairing.

A trip strip added to the clean side of the turret produced symmetric flow behind the turret for the remainder of the flow visualization study. A 1.3-cm (0.5-in) wide strip of duct tape served as the trip strip, and it ran between the base and top of the turret. The leading edge of the strip was placed approximately 100° from the front of the turret to avoid increasing the profile area of the turret. Although the flow was already turbulent upon reaching the trip strip (at higher tunnel velocities), the trip strip induced enough roughness to cause earlier separation from the otherwise smooth surface of the turret. The strip therefore matched the effective disturbances caused by the tufts on the tufted side of the turret. Figure 33 shows the difference in drag between the configurations with trip strips installed and removed.

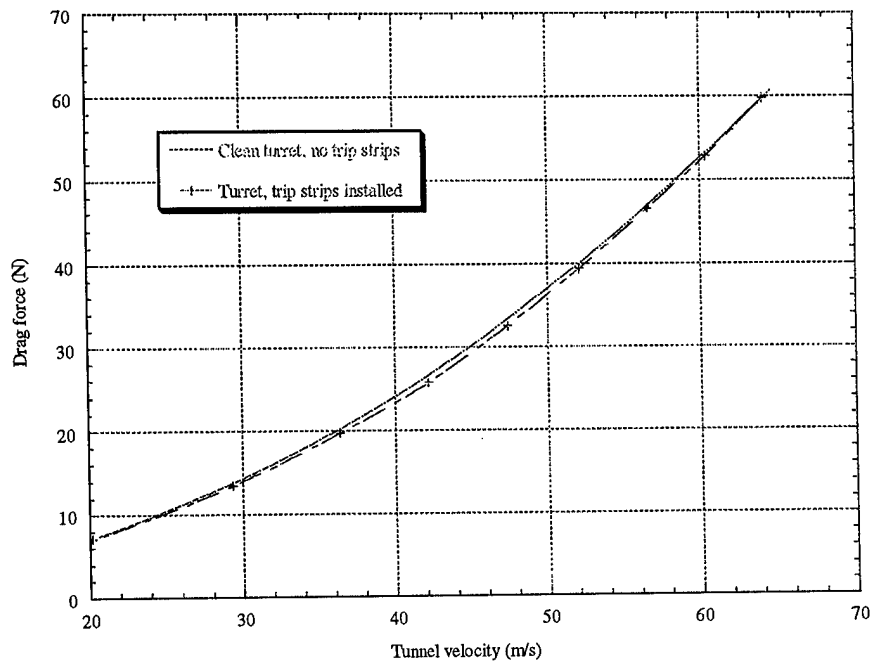


Figure 33. Drag comparison, turret with trip strips installed and removed

When force data were taken in this study, the tufts were removed and an identical trip strip was placed opposite the existing trip strip. This configuration allowed the force data to correlate as closely as possible with the conditions shown in the tuft photos. However, as shown in Figure 33, the difference in drag (the main parameter measured) was small between the runs with trip strips installed or removed. The maximum change in drag was 4% at a velocity of approximately 44 m/s (144 ft/s), but the difference became negligible at higher velocities.

6.5.2 Cavity Opening

A 0.48-cm (3/16-in) gap between the turret and surrounding cover plate was designed to allow for deflection of the turret and accurate readings from the load cell unit. Such a gap would not exist on the actual testbed aircraft, however, and the effects of having an open cavity beneath the turret model were investigated. The main concern was that the high pressure at the front and low pressure near the sides of the turret would establish a flow within the instrumentation cavity. Such a flow would give pressure relief at the front of the turret and overall lower drag readings than the true turret configuration.

To test the closed cavity, fiber tape was applied between the turret and cover plate on the underside of each. Enough slack was left in the tape to allow for deflections similar to those encountered in previous runs. Modeling clay was placed in the remaining groove around the turret to create a surface flush with the ground plane. The clean turret was tested in this configuration by observing oil flows and recording force and pressure data. The main qualitative result is shown in Figure 34, namely that the cavity opening had little effect on the drag results observed in this study.

At the highest tunnel speeds tested, the difference in drag was 3% between the cavity open and closed configurations. The difference seemed to increase with tunnel speed, however, and testing with an open cavity at much higher speeds than this study would begin to introduce high levels of error. The measured drag also indicated a decrease when the cavity was closed. The exact cause was not determined, but the stiffness of the tape and the modeling clay most likely reduced the deflection of the turret

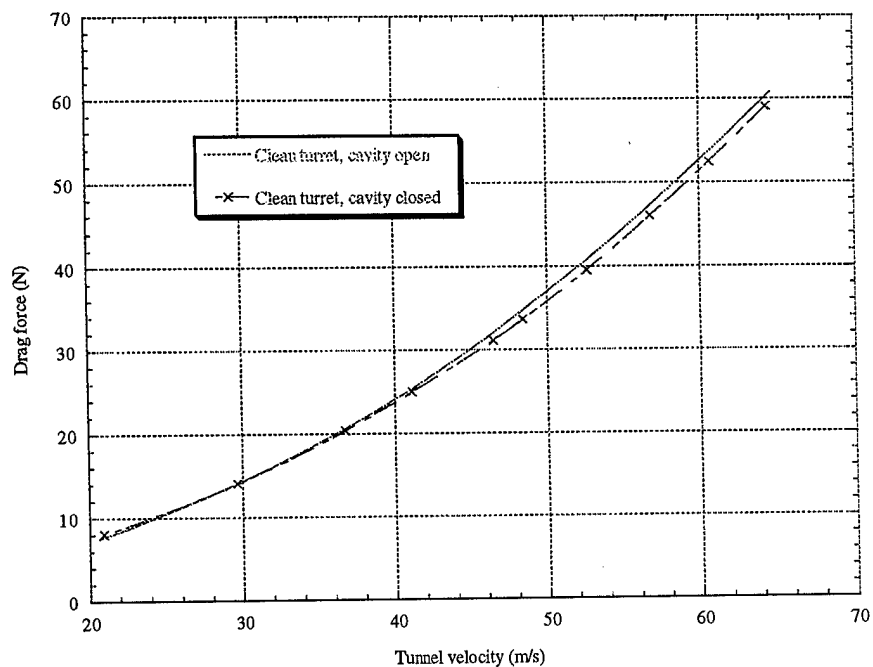


Figure 34. Drag comparison, instrumentation cavity open and closed

under wind loading and reduced the measured drag on the turret. To accurately test the effects of closing the cavity, the difficult task of sealing the cavity with an airtight yet completely flexible material must be undertaken.

Figures 35 and 36 give a visual comparison of the turret side flow with the open and closed cavity, respectively. Although the initial oil distribution in each case was not identical (resulting in different oil streak length and thickness), there were no discernible flow differences between the two cases. The main indication of flow within the cavity would be an increased upward flow along the side in Figure 35, but the side flow in each

figure was very similar. With no major flow differences or drag variations between the open and closed cavity configurations, the impact on the results of this study was minimal.

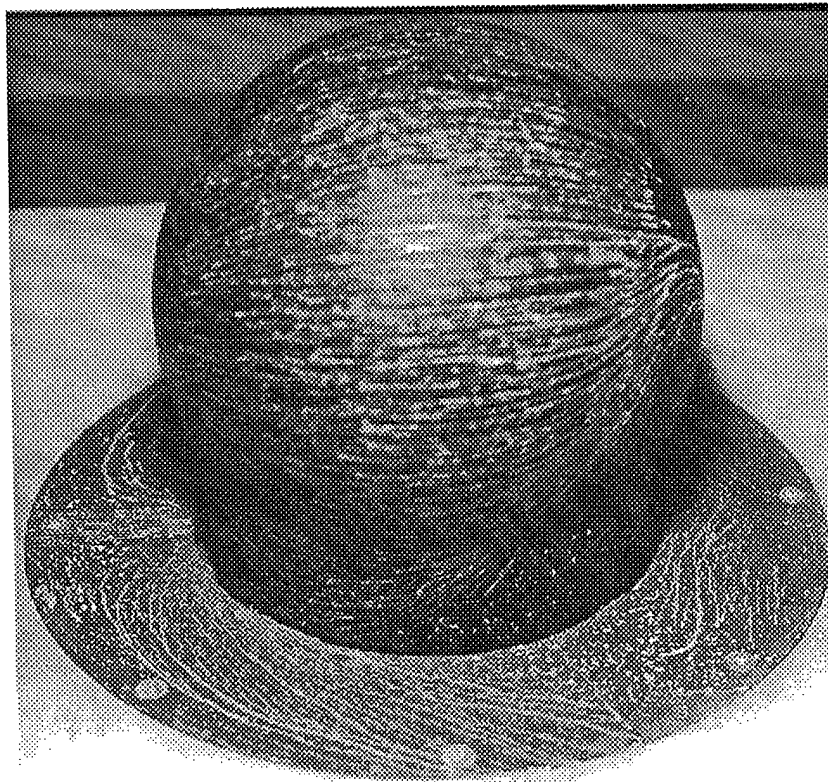


Figure 35. Oil flow, 55 m/s (180 ft/s), cavity open

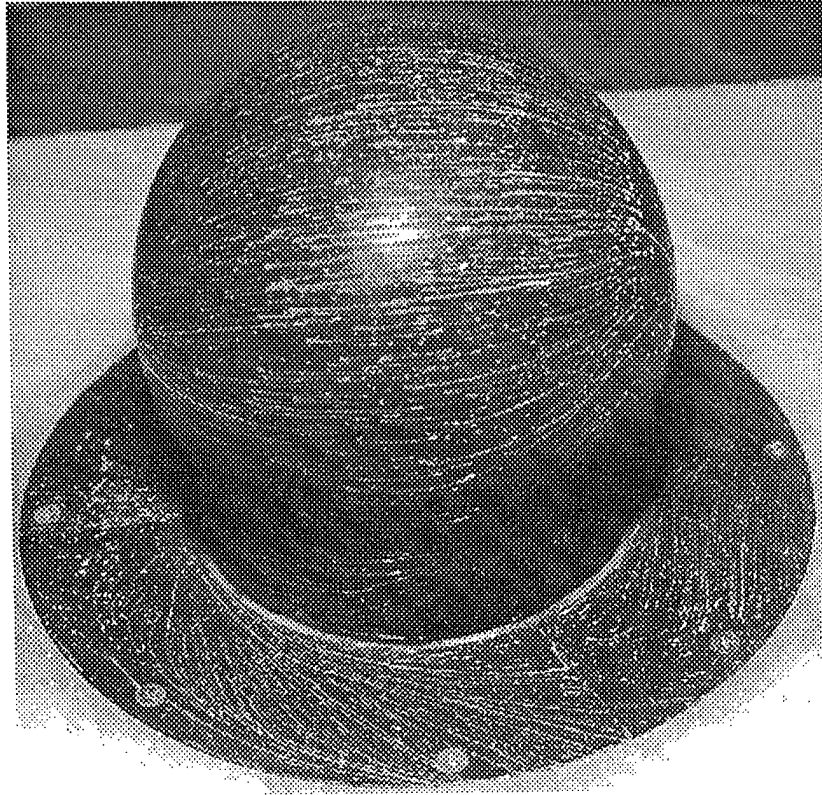


Figure 36. Oil flow, 55 m/s (180 ft/s), cavity closed

6.6 Results from Dynamic Response Pressure Transducers

During initial testing of the clean turret, the output from the four flush-mounted pressure transducers was monitored on a signal analyzer operating in Fast Fourier Transform (FFT) mode. The objective was to identify any dominant frequencies occurring in the separation region and possibly identify the frequencies at which the vortex street was shedding from the sides of the turret (by comparing the signals from the

two pressure transducers placed directly opposite each other). No such frequencies were detected, however, and the only response measured from the transducers was the shift in static pressure as the tunnel speed was varied. Any dominant frequencies within the separation region apparently had amplitudes smaller than the resolution of the pressure transducers. Since more accurate transducers were not available for this study, analyzing the dynamics within the separation region was limited to viewing the high-speed video of the tuft runs.

6.7 Error Analysis

The two main quantitative results presented in this study, the drag coefficient and pressure coefficient, were analyzed to determine the level of uncertainty inherent in their final results. The details of the calculations for this section are presented in Appendix C. Although temperature, barometric pressure, tunnel dynamic pressure, forces, moments, and turret pressure distributions were recorded, the nature of the dimensionless coefficients resulted in some of these quantities being unnecessary. As described in Appendix C, the drag coefficient only required knowledge of the drag force on the turret and the static pressure difference between atmospheric pressure and the tunnel test section. Similarly, the pressure coefficient only needed two pressure readings: the pressure difference between the pressure taps and atmospheric pressure, and the same test section pressure measurement used for the drag coefficient. The uncertainty in each of these readings and the sensitivity of the various coefficients to each reading were determined to give the total estimated uncertainties shown in Figures 37 and 38.

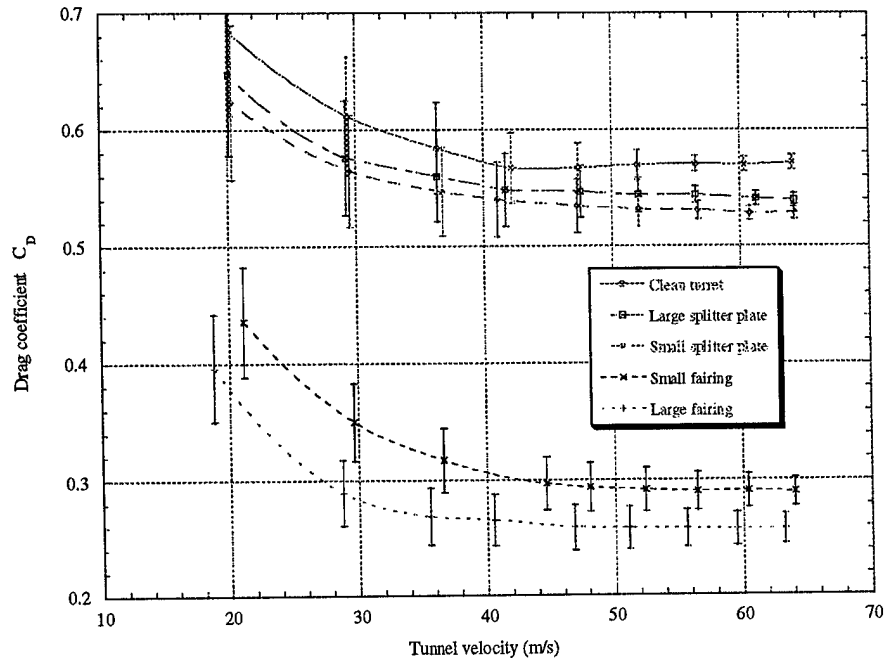


Figure 37. Uncertainty in drag coefficient measurements

As shown in Figure 37, high levels of uncertainty existed at lower tunnel speeds to an extent that the differences in drag between the clean turret and both splitter plate configurations could not be reported accurately. However, as tunnel speed increased, the uncertainty for each configuration was contained in narrower error bands. Neither fairing configuration showed an uncertainty reduction on the scale of the other configurations, but this result verified the dominant source of error in this study. The load cell unit had documented poor resolution (10% error) when subjected to applied loads on the order of 1 lb_f . When the loading was increased to 10 lb_f , this resolution improved to an error of only 1% (King, 1989: 145). At the lower tunnel velocities, drag forces were on the order of 1 lb_f , and large errors resulted. The drag forces increased tenfold on the clean turret

and splitter plate configurations at higher velocities, resulting in a significant error reduction. When the fairings were attached, however, their success in reducing drag kept the measured drag levels near the range of low resolution for the load cell unit. Unfortunately, the need to support the weight of the fairings and splitter plates in the cantilevered testing arrangement prohibited switching to weaker load cells with higher precision.

Figure 38 shows the results of the error analysis for the pressure coefficient data. The miniscule error bands for the pressure data are contained within the plot symbols for each data point. The automated (and highly accurate) PSI System produced error levels of approximately 0.5% for each pressure tap.

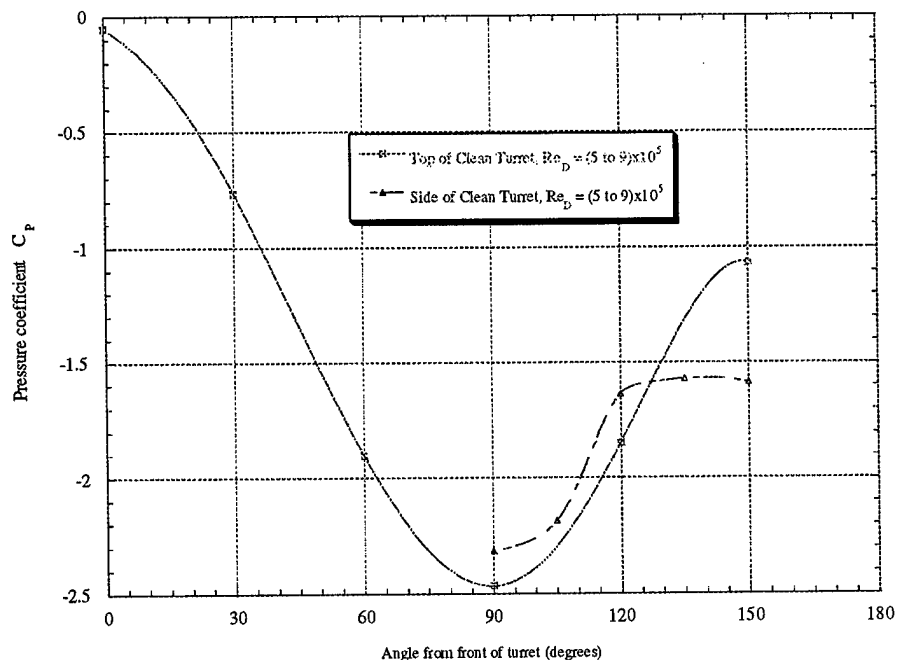


Figure 38. Uncertainty in pressure coefficient measurements

Chapter 7 - Conclusions and Recommendations

The main objective of this study was to characterize the flow field around the turret and determine a passive drag reduction technique that improved flow quality near the turret and met the viewing requirements of the laser. The three-dimensional flow over the turret was driven by dominant top vortices that shed from the top of the turret and interacted with the vortex street shed from the turret sides. This process formed a large low-pressure wake of vortices behind the turret that acted on the turret in the form of pressure drag. The splitter plates had no ability to reduce the strength of the top vortices, and minimal drag reductions resulted.

The small fairing had a cross-section that fit inside the separation region, and the flow separated from the turret slightly aft of 125° from the leading edge and did not reattach to the fairing for 1.3 diameters. This fairing eliminated 49% of the baseline turret drag while allowing an extra 30° look angle over the large fairing, but the flow quality near the turret was similar to that of the unmodified turret. The unsteady flow velocities in the separated region allowed by such a small fairing could prove even more detrimental to the flight testing of the laser system than a cleaner, high-drag configuration.

The large fairing was the most successful in reducing drag, resulting in a 55% drag reduction over the clean turret. Flow also remained attached over most of the turret when

the large fairing was attached, and the observed flow quality was much higher than any other configuration tested. No quantitative data was taken on the dynamics of the flow, but tufts, oil flow, and tuft-on-a-wire tests gave qualitative images of well-behaved flow in all areas except a very small region near the turret/fairing junction. Clearly, the large fairing sacrificed laser viewing area in exchange for the greatest drag reduction and the best separation characteristics.

The low-speed results from this study are valid for the takeoff and initial climb phases of the T-39 flight tests. However, as airspeed is increased past the point where sonic flow appears at the sides of the turret, the clean turret drag coefficient should show a sharp increase. This characteristic was documented in the wind tunnel tests of the ABL turret, during which the wind tunnel Mach number ranged from 0.6 to 0.9. At Mach 0.6, the clean turret drag coefficient was approximately 0.65, and it increased to 1.1 at Mach 0.9 (Walterick and Van Kuren, 1975). The ABL drag results correlate well with those in this study; the measured drag coefficient of the ABL turret was approximately 0.65 at Mach 0.6, and this study determined a turret drag coefficient of 0.56 at Mach 0.19.

The critical Mach number for a sphere is 0.57, above which shocks begin to form at the sides of the sphere and drag increases sharply (Shapiro, 1953). Since the mass flow forced around the top and sides of the turret in this study was greater than the flow around the corresponding areas of a sphere, the critical Mach number for the turret would be less than 0.57. Thus, the flow around the ABL turret was most likely critical even at Mach 0.6, and the drag had already begun its sharp increase. This explains the 16%

higher drag coefficient measured for the ABL (at Mach 0.6) versus the drag coefficient for the T-39 turret (at Mach 0.19). However, even at transonic airspeeds, a fairing placed behind the ABL turret was capable of reducing the baseline drag coefficient by 30%. Although the fairings tested in this study would probably become less effective at transonic speeds, the ABL results verified that drag reductions on the order of those measured in this study are quite possible.

Recommendations for future studies in this area include:

1. Testing turret/fairing configurations with a different balance system at higher velocities. The load cell unit provided adequate instrumentation in the AFIT 5-foot wind tunnel, but the cantilevered fairing arrangement placed a large moment on the load cell unit before the tunnel was even turned on. Testing the same (or modified) shapes with a more suitable balance system in a transonic tunnel would allow wind tunnel tests to more closely approximate the actual flight conditions.
2. Testing stability properties at larger sideslip angles. As mentioned in Section 6.4, the limitation of testing small sideslip angles led to the misleading result that the fairings possess an inherent tendency to yaw the airplane further into the sideslip. While this may be partially true for small sideslip angles, the ultimate tendency will be for the fairing to weathervane back into the freestream direction. Testing at a wider range of sideslip angles would yield the point at which the fairings begin to possess a stabilizing yaw moment.

3. Placing more pressure taps over the surface of the turret and fairings. Error analysis showed that the pressure measurement system used in this study was extremely accurate, possessing an uncertainty of less than 0.5%. Obtaining a finer grid of pressure measurements over the turret would allow forces and moments to be determined through integration. This would give a useful verification to any force and moment data obtained with a balance and greatly increase the validity of the findings.
4. Examine the dynamic loads acting on the turret. This type of study could provide information on vibrations, natural frequencies of the turret and turret/fairing assemblies, stability properties when exposed to wind gusts, vortex shedding frequencies, and many other circumstances encountered in actual flight conditions.

References

- Alexander, Michael G. Subsonic Wind Tunnel Testing Handbook. Flight Dynamics Directorate, Wright Laboratory, Wright-Patterson AFB OH, 1991.
- Belik, L. "The Secondary Flow about Circular Cylinders Mounted Normal to a Flat Plate," Aeronautical Quarterly: 47-54 (February 1973).
- Emsley, Howard. Aeronautical engineer, Wright Laboratory, Air Vehicles Directorate, (AFRL/VAA), Wright-Patterson AFB OH. Personal interview. 6-8 May 1998.
- Hoerner, Sighard F. Fluid-Dynamic Drag. Midland Park NJ: published by author, 1965.
- Holman, J.P. and W.J. Gajda, Jr. Experimental Methods for Engineers (Fifth Edition). New York: McGraw Hill, 1989.
- King, Brian W. Fluctuating Wind Forces Measured on a Bluff Body Extending from a Cavity. MS thesis, AFIT/GAE/ENY/89D-19. School of Aeronautical Engineering, Air Force Institute of Technology (AU), Wright-Patterson AFB OH, December 1989.
- Miller, Richard W. Flow Measurement Engineering Handbook (Third Edition). New York: McGraw Hill, 1996.
- Mullane, Richard M. An Experimental Investigation of Methods of Suppressing the Unsteady Torque Exerted on the Upper Turning Mirror of an Aircraft Mounted Coelostat Turret. MS thesis, AFIT/GAE/AE/75J-6. School of Aerospace and Mechanical Engineering, Air Force Institute of Technology (AU), Wright-Patterson AFB OH, June 1975.
- Parker, Brian A. A New Drag Measurement System for Wind Tunnel Testing of the Racing Bicycle and Rider to Determine a Low Drag Configuration. MS thesis, AFIT/GAE/ENY/94D-17. School of Aeronautical Engineering, Air Force Institute of Technology (AU), Wright-Patterson AFB OH, December 1994.
- Penix, Larry E. Flow Control About an Airborne Laser Turret. MS thesis. Naval Postgraduate School, Monterey CA, June 1982 (AD-A123 777)(NPS-67-82-007).
- Rae, William H. Jr. and Alan Pope. Low-Speed Wind Tunnel Testing (Second Edition). New York: John Wiley & Sons, 1984.
- Shapiro, A.H. The Dynamics and Thermodynamics of Compressible Fluid Flow. New York: Ronald, 1953.

Shevell, Richard S. Fundamentals of Flight (Second Edition). Englewood Cliffs NJ: Prentice Hall, 1989.

Walterick, Ronald E. and James T. Van Kuren. Wind Tunnel Tests of Fairings for an On-Gimbal Telescope Turret. Technical memorandum, AFFDL-TM-75-177 FXM. Analysis Group, Aeromechanics Division, AF Flight Dynamics Laboratory, Wright-Patterson AFB OH, November 1975.

Wolf, Nelson D. Wright Field Five-Foot Wind Tunnel. American Society of Mechanical Engineers. National historic landmark brochure. March 1995.

Yang, Wen-Jei. Handbook of Flow Visualization. Ann Arbor: Taylor & Francis, 1989.

Appendix A - Data Acquisition Apparatus

Computer: Zenith Z-station 133 MHz Pentium

Interface card: AT-GPIB Interface Card (IEEE interface)

Data Acquisition Software: Labview 4.0

Data acquisition board: National Instruments AT-MIO-64E-3

32-channel differential input board

12-bit analog to digital conversion

Input range: -10 to +10 V

Gain: 1.0

Precision: 305.18 μ V

Load Cells: Interface SM-25

Sensitivity: +/- 0.076 mm (0.003 in)

Range: 111.2 N (25 lb_f)

Precision (with gain of 50): 10% error at 1 lb_f, 1% error at 10 lb_f

Signal conditioner: Endevco 4423 Signal Conditioner and Amplifier

Gain: 50

Pressure transducers: Endevco 8507-2 peizoresistive pressure transducer

Range: 2 psig

Sensitivity: 132.2 mV/psi

Static pressure measurement system: Pressure Systems Inc. (PSI) System 8400

8420 SDU 14-bit analog to digital conversion module

8433 Pressure Calibration Unit (PCU)

Range: 1 psi differential (psid)

ESP-32 Electronic Pressure Scanner

Range: +/- 20 inches water

Accuracy: +/- 0.1% of full scale reading = 0.02 inches water

Tunnel static pressure transducer:

MKS Instruments, Inc. 223BD-00100ABB differential pressure transducer

Range: 100 torr

Accuracy: +/- 0.0426 inches water

MKS PDR-C-2C Power Supply Readout

Tunnel temperature measurement:

Omega Type-T thermocouple

Accuracy (at 25 °C): +/- 0.5 °C

Omega DP25-TC-A Thermocouple Indicator

Appendix B - Load Cell Unit

The load cell unit (LCU) measured the six loading components F_x , F_y , F_z , M_x , M_y , and M_z through eight load cells arranged symmetrically beneath the turret model. The voltages from the eight load cells were transformed into six combined voltages EC_1 , EC_2 , EC_3 , EC_4 , EC_5 , and EC_6 , corresponding to the loading components listed above. A diagram of the individual load cells within the LCU is shown in Figure 39 and the composition of the combined voltages is defined in Table 2.

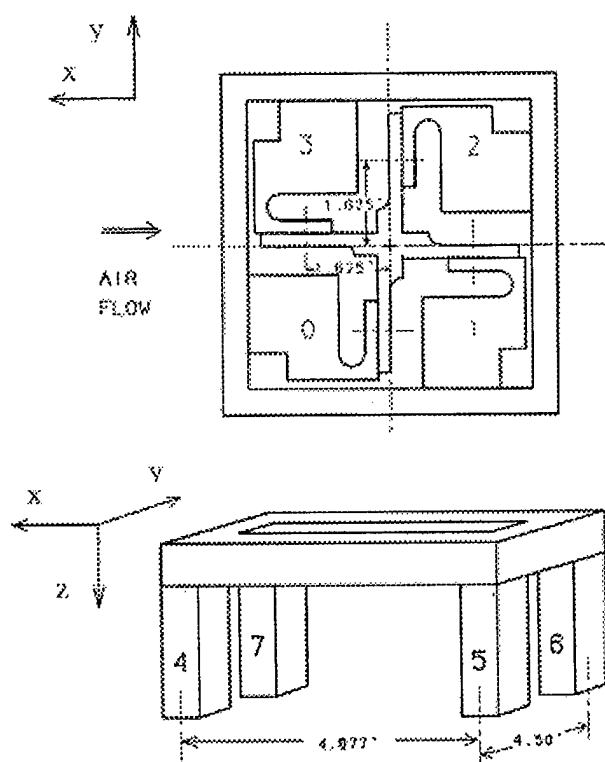


Figure 39. Individual load cell placement within the LCU (King, 1989: 27)

Table 2. Load cell output voltage definitions (King, 1989: 116)

<u>Voltage Combination</u>	<u>Load Cell Responses</u>
$EC_1 = (E_2 - E_0) \rightarrow F_x$	Positive X Force $E_0 = -$ $E_2 = +$
$EC_2 = (E_1 - E_3) \rightarrow F_y$	Positive Y Force $E_1 = +$ $E_3 = -$
$EC_3 = -(E_4 + E_5 + E_6 + E_7) \rightarrow F_z$	Positive Z Force $E_4 = - \quad E_6 = -$ $E_5 = - \quad E_7 = -$
$EC_4 = (E_4 + E_5) - (E_6 + E_7) \rightarrow M_x$	Positive X Moment $E_4 = + \quad E_6 = -$ $E_5 = + \quad E_7 = -$
$EC_5 = (E_4 + E_7) - (E_5 + E_6) \rightarrow M_y$	Positive Y Moment $E_4 = + \quad E_6 = -$ $E_5 = - \quad E_7 = +$
$EC_6 = -(E_0 + E_1 + E_2 + E_3) \rightarrow M_z$	Positive Z Moment $E_0 = - \quad E_2 = -$ $E_1 = - \quad E_3 = -$

Calibrations for each of the six loading components produced a matrix such that

$$\begin{bmatrix} \frac{\partial EC_1}{\partial F_x} & \frac{\partial EC_2}{\partial F_x} & \frac{\partial EC_3}{\partial F_x} & \frac{\partial EC_4}{\partial F_x} & \frac{\partial EC_5}{\partial F_x} & \frac{\partial EC_6}{\partial F_x} \\ \frac{\partial EC_1}{\partial F_y} & \frac{\partial EC_2}{\partial F_y} & \frac{\partial EC_3}{\partial F_y} & \frac{\partial EC_4}{\partial F_y} & \frac{\partial EC_5}{\partial F_y} & \frac{\partial EC_6}{\partial F_y} \\ \frac{\partial EC_1}{\partial F_z} & \frac{\partial EC_2}{\partial F_z} & \frac{\partial EC_3}{\partial F_z} & \frac{\partial EC_4}{\partial F_z} & \frac{\partial EC_5}{\partial F_z} & \frac{\partial EC_6}{\partial F_z} \\ \frac{\partial EC_1}{\partial M_x} & \frac{\partial EC_2}{\partial M_x} & \frac{\partial EC_3}{\partial M_x} & \frac{\partial EC_4}{\partial M_x} & \frac{\partial EC_5}{\partial M_x} & \frac{\partial EC_6}{\partial M_x} \\ \frac{\partial EC_1}{\partial M_y} & \frac{\partial EC_2}{\partial M_y} & \frac{\partial EC_3}{\partial M_y} & \frac{\partial EC_4}{\partial M_y} & \frac{\partial EC_5}{\partial M_y} & \frac{\partial EC_6}{\partial M_y} \\ \frac{\partial EC_1}{\partial M_z} & \frac{\partial EC_2}{\partial M_z} & \frac{\partial EC_3}{\partial M_z} & \frac{\partial EC_4}{\partial M_z} & \frac{\partial EC_5}{\partial M_z} & \frac{\partial EC_6}{\partial M_z} \end{bmatrix} \begin{Bmatrix} F_x \\ F_y \\ F_z \\ M_x \\ M_y \\ M_z \end{Bmatrix} = \begin{Bmatrix} EC_1 \\ EC_2 \\ EC_3 \\ EC_4 \\ EC_5 \\ EC_6 \end{Bmatrix} \quad (11)$$

or $[A]\{F\} = \{EC\}$ (12)

where, for example, $\frac{\partial EC_1}{\partial F_x}$ is the change in the combined voltage EC_1 due to a load in the x-direction, F_x .

A full matrix in Equation (11) would include all secondary or off-axis responses from the LCU to a particular loading. For example, any change in EC_1 due to a moment about the x-axis would be contained in element (4,1) of $[A]$. However, calibrations in this study determined that secondary responses only appeared when the direction of the force application was not perfectly aligned with the axis of the LCU. Accurate calibrations made these secondary responses negligible as shown in the calibration curves contained in this appendix. The resulting $[A]$ matrix was a diagonal matrix and was easily inverted to calculate the forces once given the combined voltages.

The only sets of loading components that were loosely coupled were F_x & M_y and F_y & M_x . A force in the x-direction caused a moment about the y-axis and vice versa. This is shown in all the force calibration figures as two lines with noticeable nonzero slopes. Although the two were coupled, the force (F_x or F_y) could be determined independent of the moment (M_y or M_x). For example, Figures 42 and 43 show the calibration curves for negative-x and negative-x (high) force applications. These calibrations were carried out in exactly the same manner, but the forces were applied to the turret at different heights above the ground plane to test the coupling of F_x and M_y . In both figures, the slope of EC_1 (corresponding to F_x) is nearly equal. This slope could be used to calculate the drag force acting on the turret regardless of the height at which the force was acting.

Since the forces were applied at different heights in the two figures, the slope of EC_5 (corresponding to M_y) varied between the two figures. When the same data was plotted against the applied moments (see Figures 44 and 45), the slopes of EC_5 were equal and the slopes of EC_1 varied between figures. Thus, to determine the forces and moments acting on the turret in a given direction, the force (say, F_x) was first determined independently using EC_1 . Similarly, the total M_y was determined independently using EC_5 . Then, to calculate M_y acting about the surface of the ground plane, the moment caused by F_x acting at the surface of the ground plane (a known distance above the LCU centroid) was subtracted from the total M_y . All calibrations performed in this study are presented in Figures 42 through 60.

Figures 40 and 41 contain two representative check loadings applied before and after testing took place. No shifts in output from the LCU were evident in the check loadings.

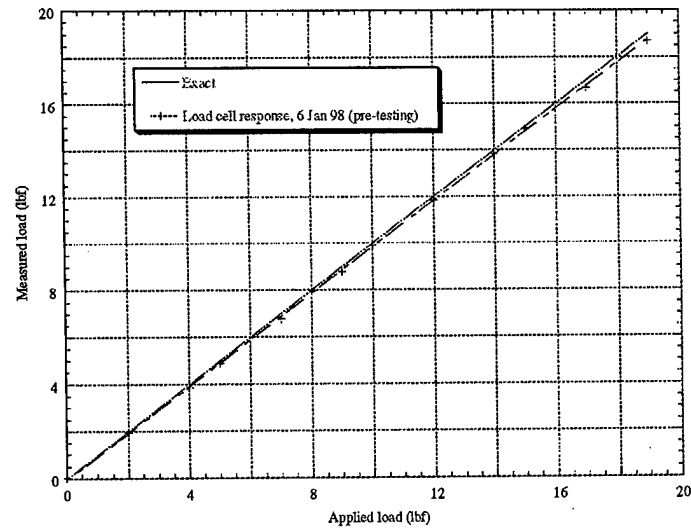


Figure 40. Drag check-load prior to testing

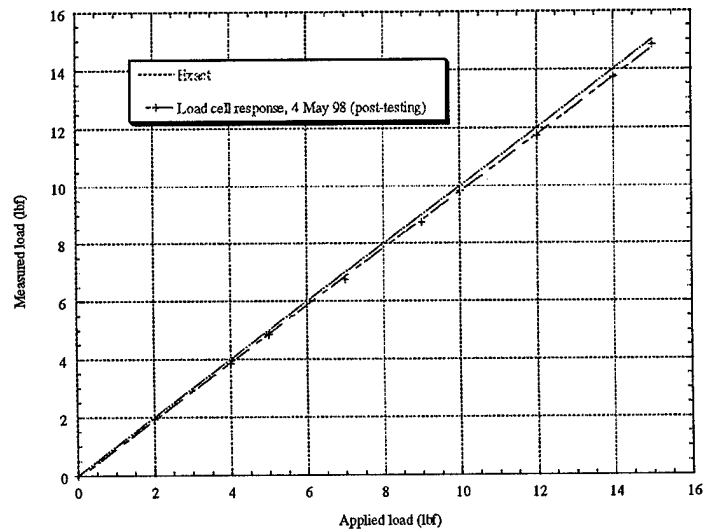


Figure 41. Drag check-load following test completion

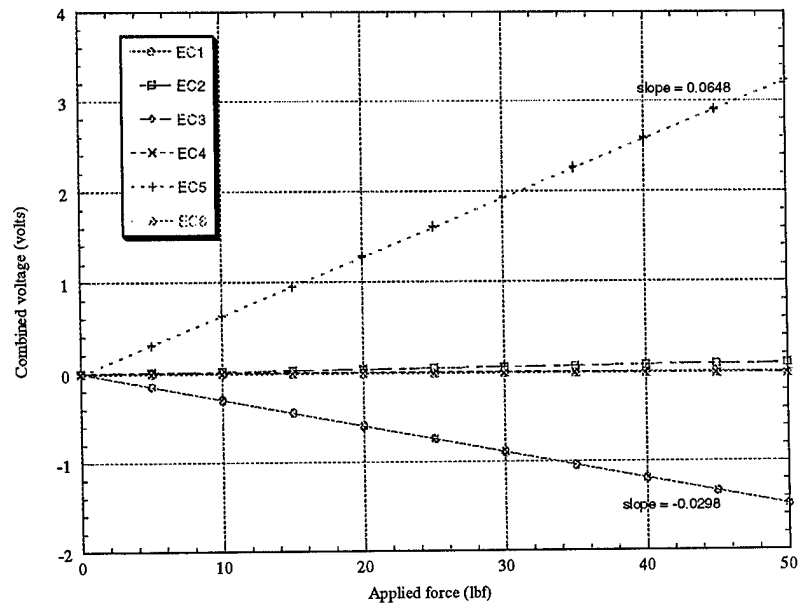


Figure 42. Negative F_x calibration

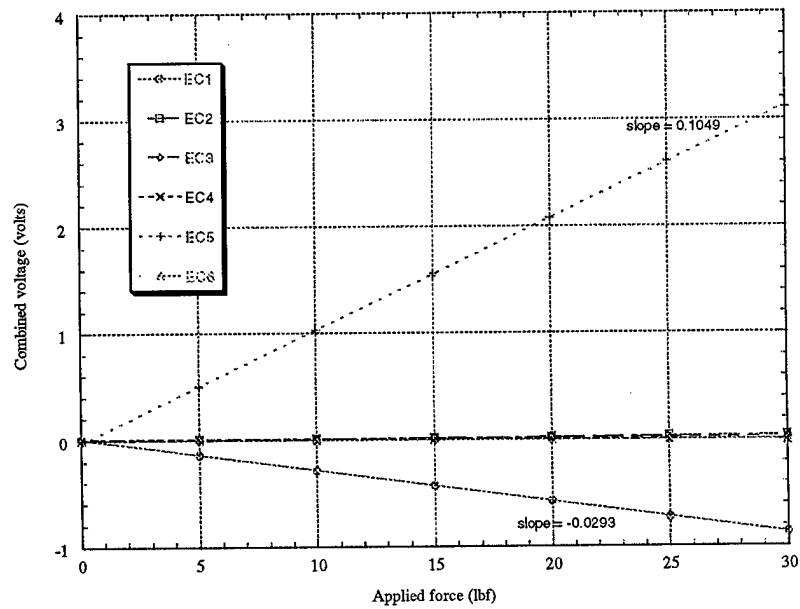


Figure 43. Negative F_x (high) calibration

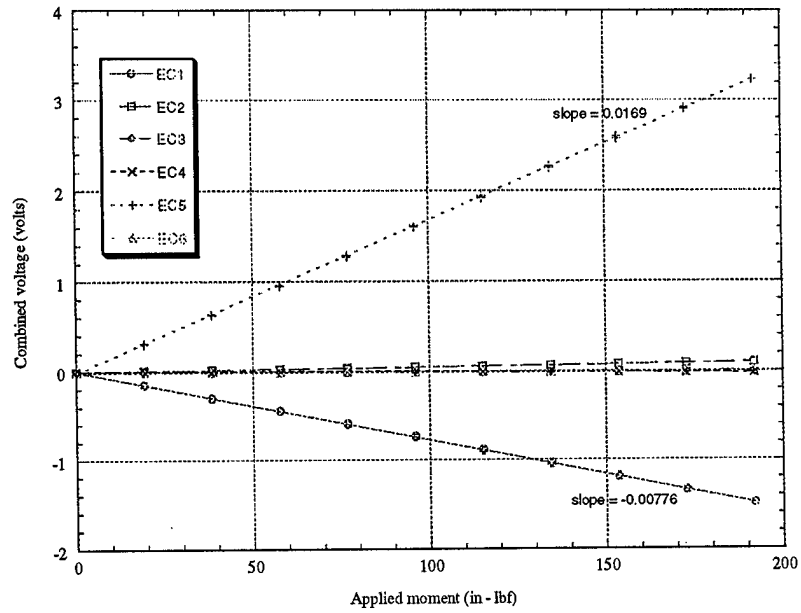


Figure 44. Positive M_y calibration (negative F_x applied)

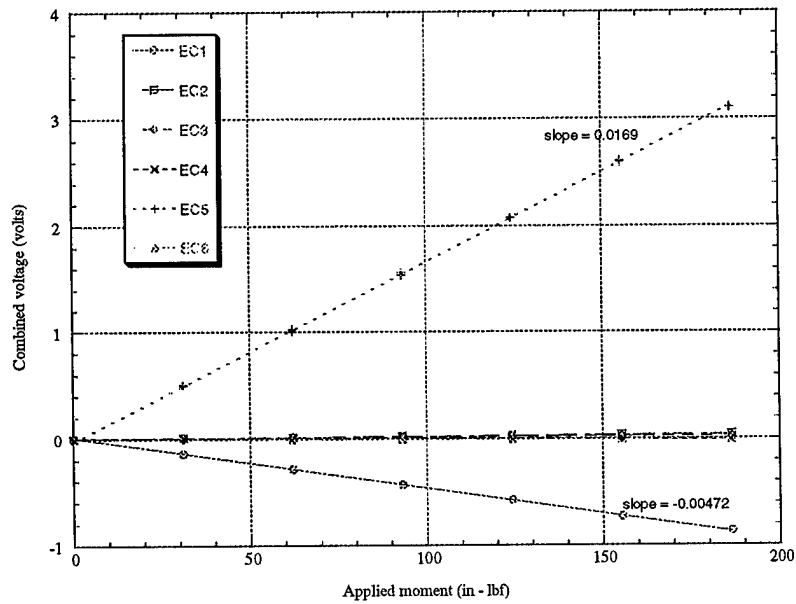


Figure 45. Positive M_y calibration (negative F_x {high} applied)

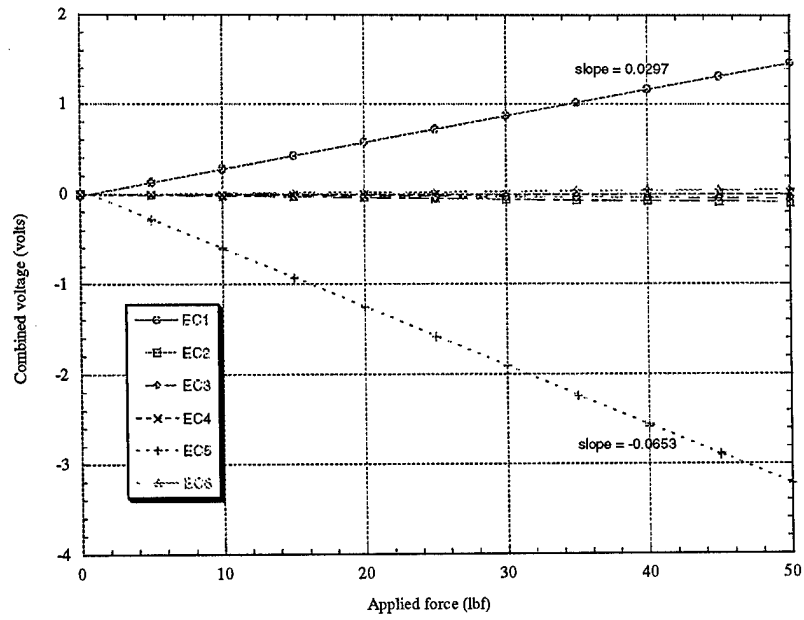


Figure 46. Positive F_x calibration

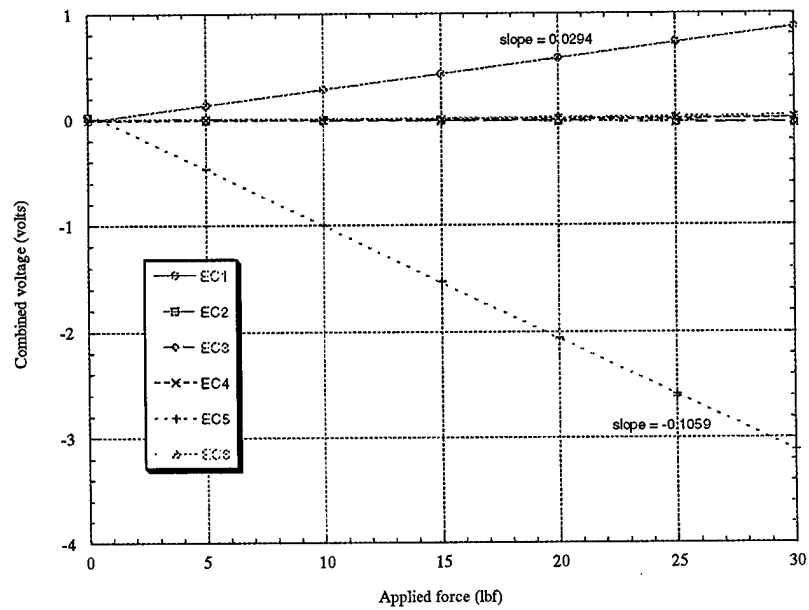


Figure 47. Positive F_x (high) calibration

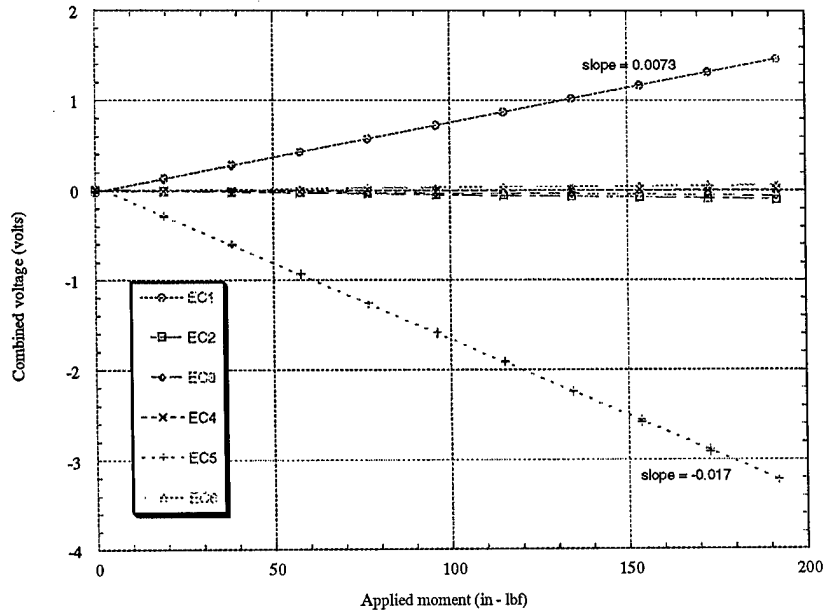


Figure 48. Negative M_y calibration (positive F_x applied)

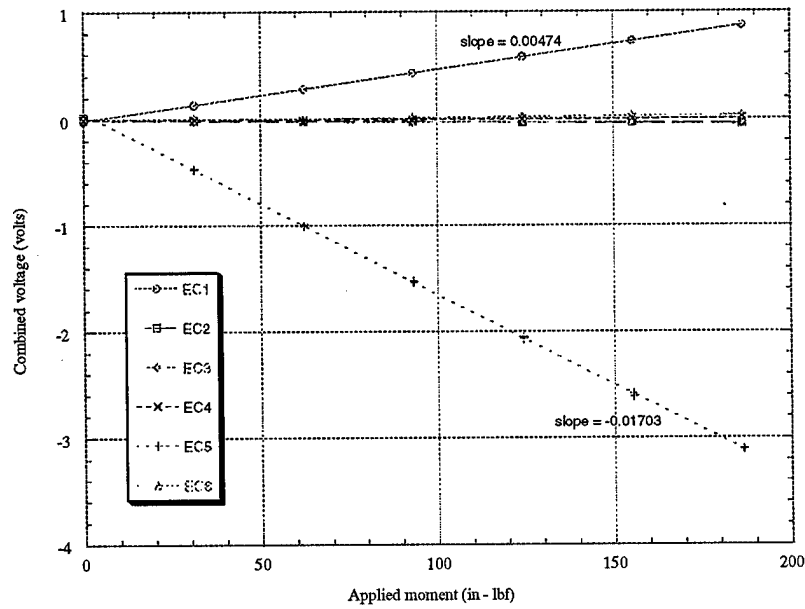


Figure 49. Negative M_y calibration (positive F_x {high} applied)

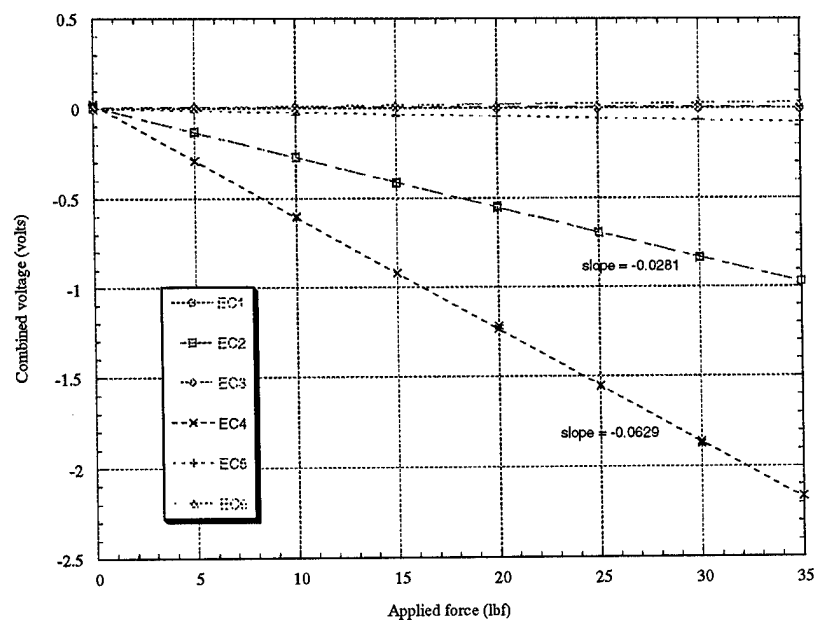


Figure 50. Negative F_y calibration

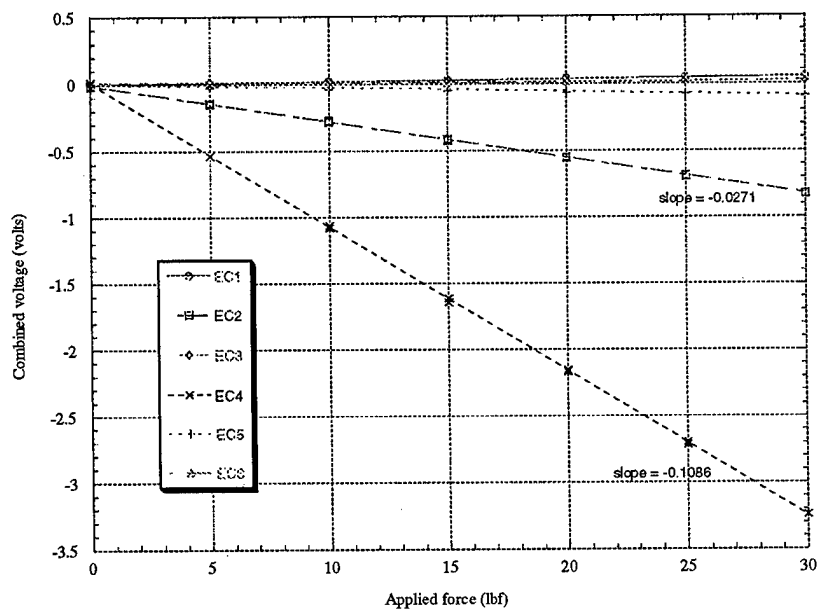


Figure 51. Negative F_y (high) calibration

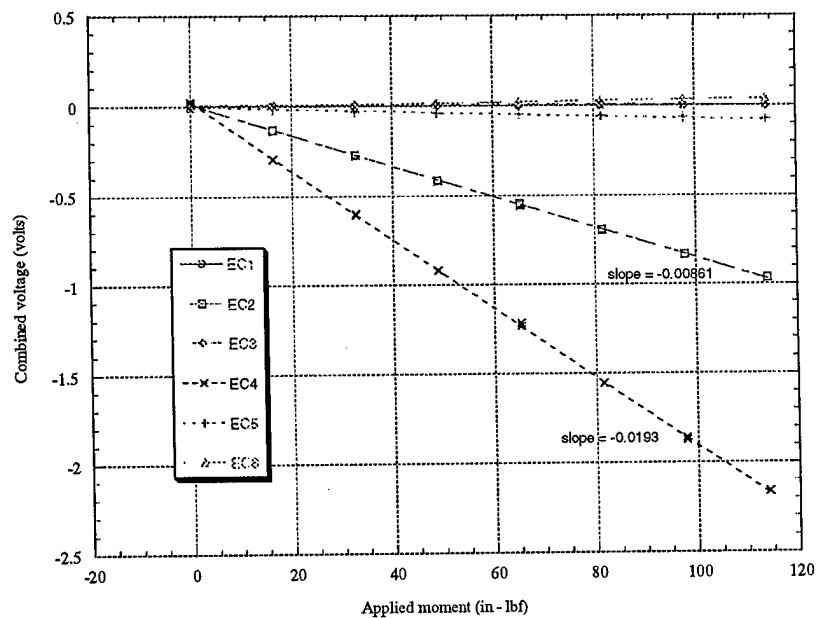


Figure 52. Negative M_x calibration (negative F_y applied)

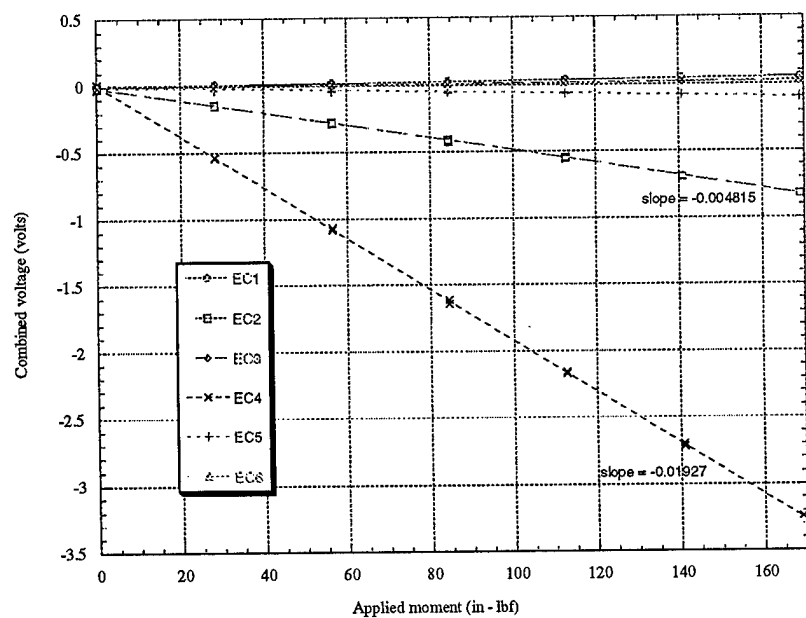


Figure 53. Negative M_x calibration (negative F_y {high} applied)

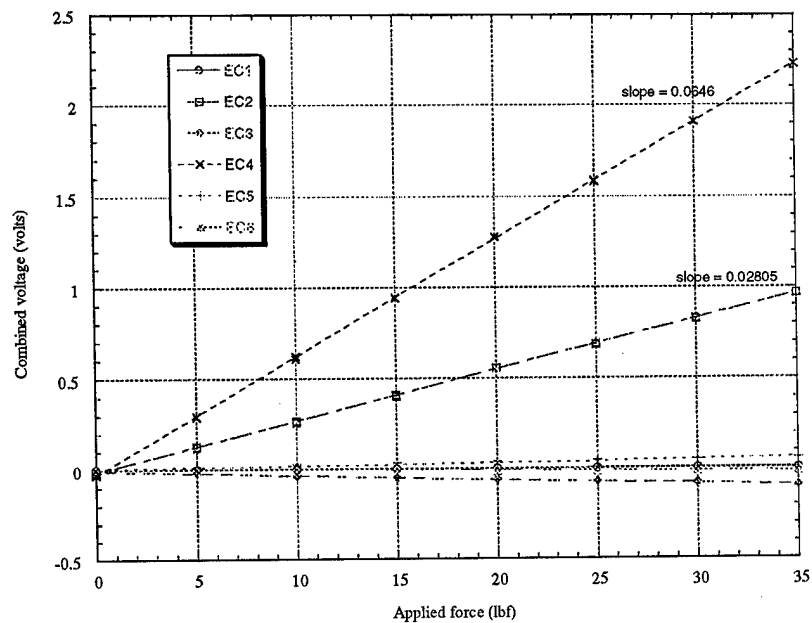


Figure 54. Positive F_y calibration

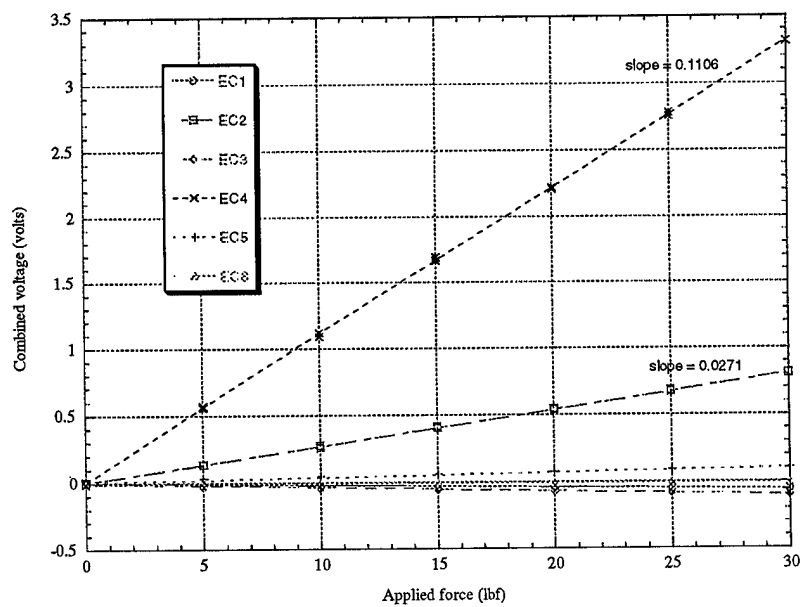


Figure 55. Positive F_y (high) calibration

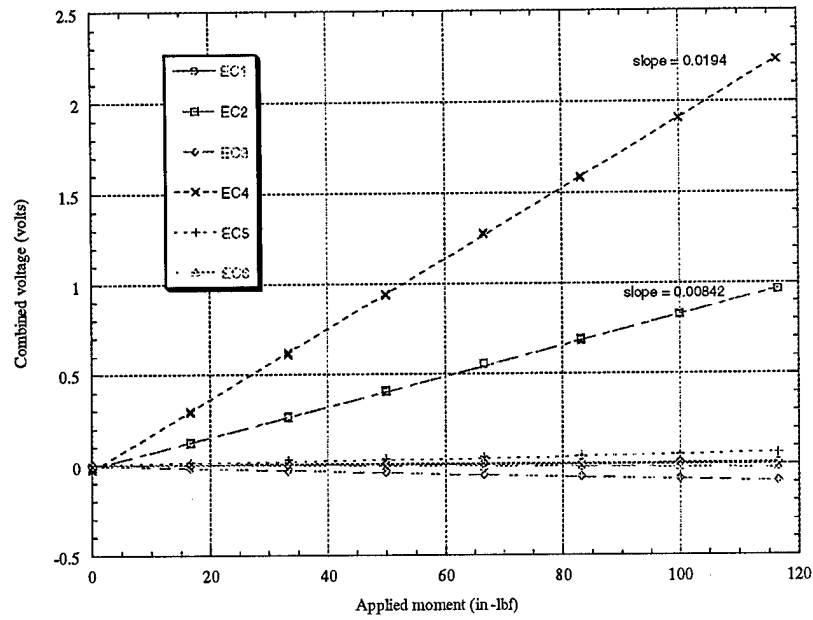


Figure 56. Positive M_x calibration (positive F_y applied)

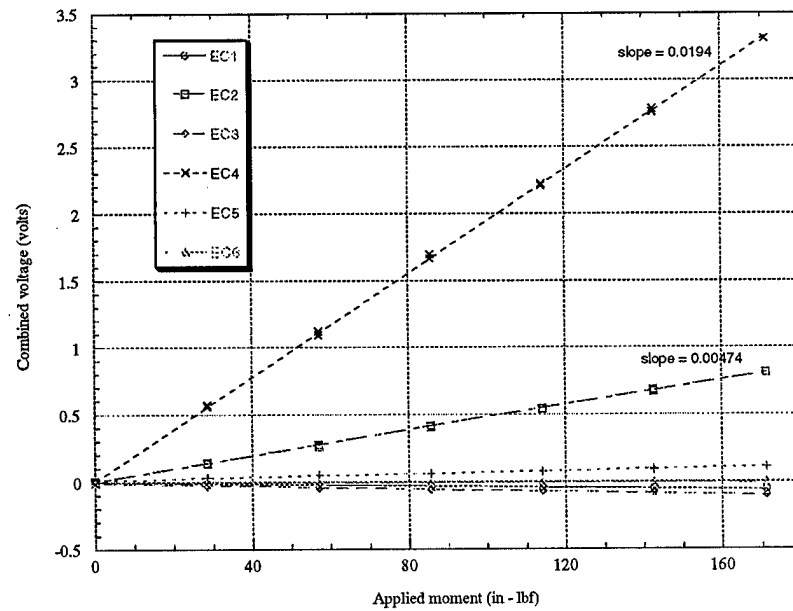


Figure 57. Positive M_x calibration (positive F_y {high} applied)

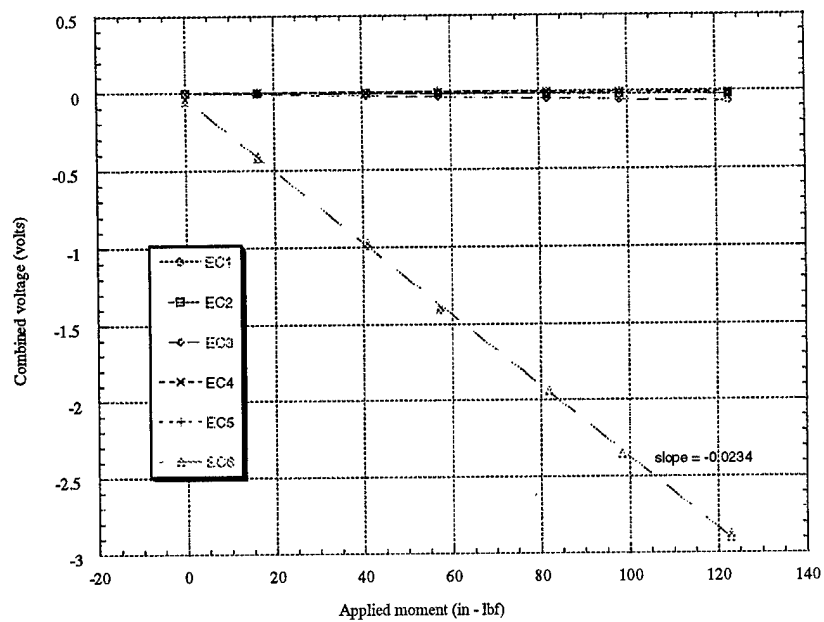


Figure 58. Negative M_z calibration

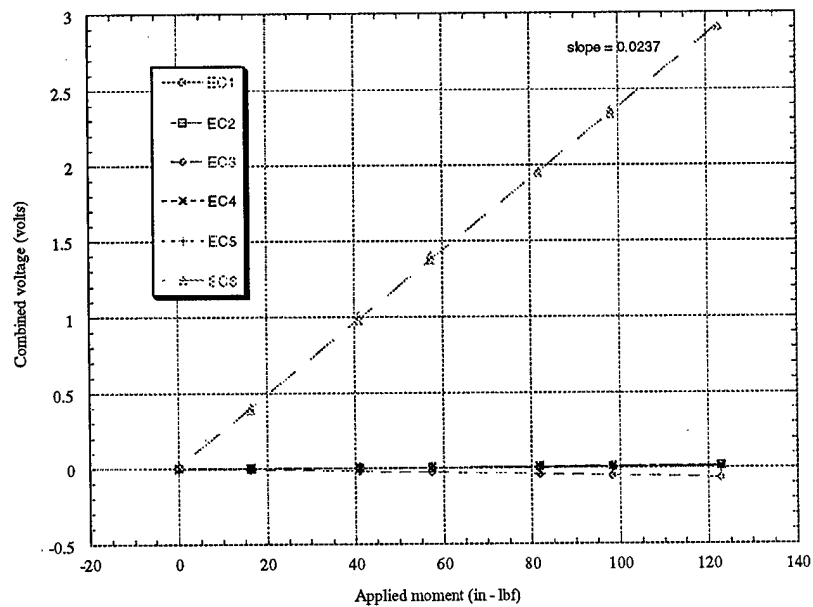


Figure 59. Positive M_z calibration

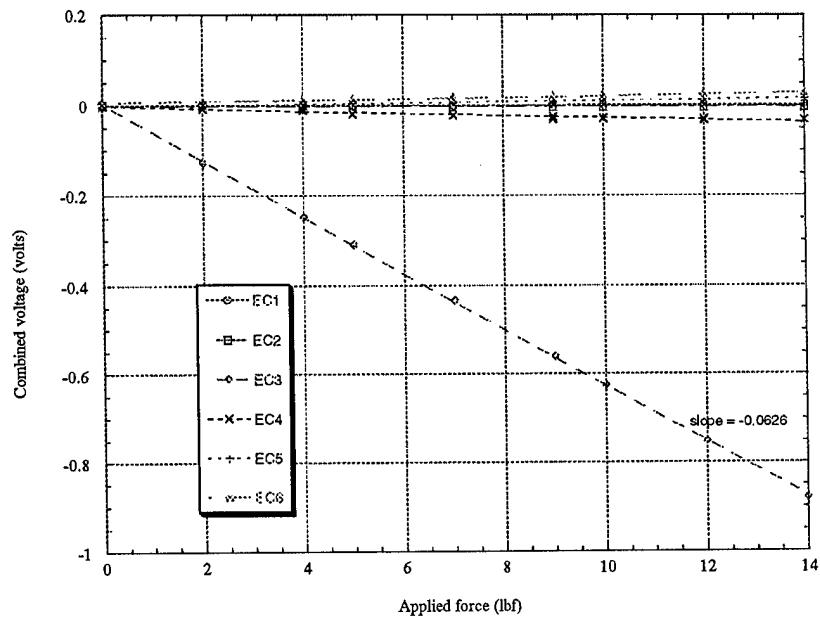


Figure 60. Positive F_z calibration

Appendix C - Error Analysis

The uncertainty in the experimental results of this study was examined using the method presented by Kline and McClintock (Holman, 1989: 41). In this method, if the final result R is a function of independent variables x_1 through x_n ,

$$R = R(x_1, x_2, x_3, \dots, x_n) \quad (13)$$

the uncertainty in the result w_R is a function of the uncertainty in each independent variable w_i and the sensitivity of R to a change in each variable:

$$w_R = \left[\left(\frac{\partial R}{\partial x_1} \cdot w_1 \right)^2 + \left(\frac{\partial R}{\partial x_2} \cdot w_2 \right)^2 + \dots + \left(\frac{\partial R}{\partial x_n} \cdot w_n \right)^2 \right]^{1/2} \quad (14)$$

To apply this method to the drag coefficient, the fundamental measured variables must first be substituted for each derived quantity in the drag coefficient expression:

$$C_D = \frac{D}{\frac{1}{2} \rho V^2 \cdot S} = \frac{EC_1 \cdot \left(\frac{\partial EC_1}{\partial F_x} \right)^{-1}}{\frac{\rho}{2} \left((1 + \epsilon_t) \sqrt{\frac{2}{\rho} (P_{atm} - P_{tun})} \right)^2 \cdot S} = \frac{EC_1 \cdot \left(\frac{\partial EC_1}{\partial F_x} \right)^{-1}}{(1 + \epsilon_t)^2 (P_{atm} - P_{tun}) \cdot S} \quad (15)$$

Only two measurements were needed to calculate the drag coefficient: the voltage from the load cell unit (corresponding to the drag force) and the tunnel dynamic pressure (used to calculate the tunnel velocity). The partial derivatives of C_D with respect to these quantities are shown below.

$$\frac{\partial C_D}{\partial EC_1} = \frac{\left(\frac{\partial EC_1}{\partial F_x}\right)^{-1}}{(1 + \varepsilon_t)^2 \cdot (P_{atm} - P_{tun}) \cdot S} \quad (16)$$

$$\frac{\partial C_D}{\partial (P_{atm} - P_{tun})} = \frac{-EC_1 \cdot \left(\frac{\partial EC_1}{\partial F_x}\right)^{-1}}{(1 + \varepsilon_t)^2 \cdot S \cdot (P_{atm} - P_{tun})^2} \quad (17)$$

These values are placed into the following expression with the uncertainties in the load cell voltage and the tunnel dynamic pressure to give the uncertainty in the drag coefficient:

$$w_{C_D} = \left[\left(\frac{\partial C_D}{\partial EC_1} \cdot w_{EC_1} \right)^2 + \left(\frac{\partial C_D}{\partial (P_{atm} - P_{tun})} \cdot w_{(P_{atm} - P_{tun})} \right)^2 \right]^{1/2} \quad (18)$$

The nominal and uncertainty values for the drag coefficient at several tunnel speeds are given in Table 3.

Table 3. Drag coefficient error

Tunnel speed (m/s)	C _D , nominal value	C _D , uncertainty	Error (%)
20	0.684	0.072	10.5
36.4	0.584	0.039	6.68
52.1	0.570	0.0128	2.25
64.1	0.572	0.00632	1.1

The error was apparently driven by the resolution of the load cell unit, which was listed as having a 10% error under a 1 lb_f loading and a 1% error under a 10 lb_f loading (King, 1989:145). At the lowest tunnel speed listed in Table 3, the drag force measured by the load cell unit was 1.61 lb_f, and the calculated error in the drag coefficient was 10.5%. At the high end of the velocity range in Table 3, the measured drag force was 13.4 lb_f, and the error in the drag coefficient was 1.1%. Figure 37 summarizes the above results for each configuration tested

The procedure for calculating the error in the pressure coefficient followed exactly from the procedure outlined above. Similar to the above analysis, the pressure coefficient also only relied on two quantities. One was the difference between atmospheric pressure and the pressure measured at various locations on the turret surface, and the other was the difference between atmospheric pressure and the pressure measured in the tunnel test section. In these calculations, however, the accuracy of the PSI System was much higher than the LCU (See Appendix A) and the uncertainty was reduced to negligible levels. Table 4 lists the nominal and uncertainty values of the pressure coefficient at various tap locations, and Figure 38 summarizes the uncertainty results for the pressure coefficient.

Table 4. Pressure coefficient error

Pressure Tap #	C_p , nominal value	C_p , uncertainty	Error
1	-0.0523	0.00261	4.99%
3	-1.903	0.00910	0.48%
5	-1.850	0.00887	0.48%
7	-2.317	0.01095	0.47%
9	-1.636	0.00795	0.48%
11	-1.587	0.00774	0.49%

In the tuft photos contained in Chapter 6, separation was determined by observing the motion of individual tufts and noting the angle from the front of the turret at which rapid oscillations began. Even though the tufts were placed head-to-tail on the turret surface, separation could shift to different points along a tuft length without creating any noticeable differences in the tuft motion. The length of each tuft corresponded to approximately 10° of arc length on the turret surface, and the uncertainty in the separation measurements was determined to be 50% of a tuft's equivalent arc length, namely $\pm 5^\circ$.

Vita

Lieutenant Christopher H. Snyder was born in Canton, Ohio on June 7, 1974. He graduated valedictorian from Carrollton High School in Carrollton, Ohio in 1992 and subsequently attended Cornell University in Ithaca, New York. Upon graduating with a bachelor's degree in Mechanical Engineering in 1996, he was recognized as a distinguished graduate from Reserve Officer Training Corps (ROTC) and received a regular commission as a Second Lieutenant in the United States Air Force. His first assignment was to the Dayton Area Graduate Studies Institute (DAGSI) through the Civilian Institution (CI) program, where he studied Aeronautical Engineering under a Theodore von Karman scholarship.

Permanent Address: 2223 Montero Rd. N.E.
Carrollton, OH 44615